AD_____

AWARD NUMBER: W81XWH-04-1-0446

TITLE: Comparison of the Specificity of MR-EIT and Dynamic Contrast-Enhanced MRI in Breast Cancer

PRINCIPAL INVESTIGATOR: Ozlem Birgul, Ph.D.

CONTRACTING ORGANIZATION: University of California, Irvine
Irvine, California 90297-7600

REPORT DATE: May 2006

TYPE OF REPORT: Annual

PREPARED FOR: U.S. Army Medical Research and Materiel Command
Fort Detrick, Maryland 21702-5012

REPORT DOCUMENTATION PAGE

Form Approved
OMB No. 0704-0188

1. REPORT DATE *(DD-MM-YYYY)*	**2. REPORT TYPE**	**3. DATES COVERED** *(From - To)*
01-05-2006	Annual	16 Apr 2005 – 15 Apr 2006

4. TITLE AND SUBTITLE

Comparison of the Specificity of MR-EIT and Dynamic Contrast-Enhanced MRI in Breast Cancer

5a. CONTRACT NUMBER

5b. GRANT NUMBER
W81XWH-04-1-0446

5c. PROGRAM ELEMENT NUMBER

6. AUTHOR(S)

Ozlem Birgul, Ph.D.

E-Mail: obirgul@uci.edu

5d. PROJECT NUMBER

5e. TASK NUMBER

5f. WORK UNIT NUMBER

7. PERFORMING ORGANIZATION NAME(S) AND ADDRESS(ES)

University of California, Irvine
Irvine, California 90297-7600

8. PERFORMING ORGANIZATION REPORT NUMBER

9. SPONSORING / MONITORING AGENCY NAME(S) AND ADDRESS(ES)
U.S. Army Medical Research and Materiel Command
Fort Detrick, Maryland 21702-5012

10. SPONSOR/MONITOR'S ACRONYM(S)

11. SPONSOR/MONITOR'S REPORT NUMBER(S)

12. DISTRIBUTION / AVAILABILITY STATEMENT
Approved for Public Release; Distribution Unlimited

13. SUPPLEMENTARY NOTES

14. ABSTRACT

It is possible to detect locations of lesions accurately in breast cancer using techniques such as x-ray mammogram accurately; however, the specificity of current techniques is low. Since the conductivity values of malignant, benign, and normal tissues are significantly different, this information can be used in classification. Current conductivity imaging techniques can only provide low-resolution images and fail in extreme cases. Magnetic resonance-electrical impedance tomography (MREIT) is a new modality that can reconstruct high-resolution conductivity images. In this study, we propose the use of MREIT for improving accuracy of breast cancer classification. In the second year of this multidisciplinary post-doctoral training grant, the principal investigator continued to acquire training in breast cancer biology by attending several seminars. She also practiced experimentation and analysis procedures for dynamic contrast enhanced-magnetic resonance imaging (DCE-MRI) that will be used in the comparative studies in the last year of the project. Simultaneously, the hardware and pulse sequence that is capable of measuring magnetic flux density with low amplitude currents are developed. In our preliminary animal experiments, in vivo MREIT imaging at a safe current level of 1mA is achieved.

15. SUBJECT TERMS
electrical impedance tomography (EIT), dynamic contrast-enhanced magnetic resonance imaging (DCE-MRI), breast cancer

16. SECURITY CLASSIFICATION OF:			**17. LIMITATION OF ABSTRACT**	**18. NUMBER OF PAGES**	**19a. NAME OF RESPONSIBLE PERSON**
a. REPORT	**b. ABSTRACT**	**c. THIS PAGE**			USAMRMC
U	U	U	UU	58	**19b. TELEPHONE NUMBER** *(include area code)*

Table of Contents

INTRODUCTION

Background

Electrical properties of malignant and normal tissues show different characteristics. The electrical impedance of malignant tumors decreases by a factor of 20-40 times with respect to the normal or benign tissues [1]. Therefore, electrical conductivity information, which is inversely related to impedance, can be used in tumor detection and characterization. At the present time, well-established breast screening methods have high sensitivity but suffer from poor or variable specificity and fail in dense breast tissues. Accurate measurement of conductivity is a potential approach to achieve higher specificity rates compared to the currently used techniques. Electrical Impedance Scanning (EIS) reconstructs conductivity inside the breast for tumor characterization, however, suffers from low resolution and fails to detect tumors that are far away from the surface [2]. In EIS, voltage measurements are used to find the conductivity. These measurements can only be made from periphery (non-invasively) and number of measurements are limited, and thus has low and space dependent resolution. In this project, we are investigating the efficacy of a new conductivity imaging technique, referred to as Magnetic Resonance-Electrical Impedance Tomography (MREIT) for breast imaging [3-5]. In MREIT, current is injected to the object and magnetic flux distribution is measured from inside the sample using MRI. Then the inverse problem of finding the conductivity distribution inside the object from measurements is solved using various reconstruction approaches, mostly based on finite element method (FEM). Measurement of magnetic field distribution not only will enhance the resolution of conductivity images but also will provide a uniform sensitivity throughout the imaging region.

In this project, we will also compare the performance of the new technique with Dynamic Contrast-Enhanced Magnetic Resonance Imaging (DCE-MRI) [6, 7]. Towards this aim, we will first improve the quality of the MREIT technique in terms of experimental setup and reconstruction algorithms. There are two major hypotheses in this proposal: (1) One can reconstruct high resolution conductivity images using the 3D MREIT technique; (2) High resolution conductivity images will result in higher specificity in breast cancer than the DCE-MRI with currently used clinical contrast agents.

Recent advancements in the field

In this section, related works published in the literature during last year are summarized in chronological order. Works published from this grant are not listed here but covered in reportable outcome section and are referred to in the body section.

- Electrical conductivity images of biological tissue phantoms in MREIT (Oh *et.al* [8]): In this study, the researchers used agar phantoms containing porcine muscle and chicken breast and acquired magnetic flux density images using a 3T magnet. The amplitude of current pulses was either 120mA (pulse width = 10msec) or 480mA (10msec) and harmonic B_Z gradient algorithm was used for conductivity reconstruction.
- Estimation of electrical conductivity distribution within the human head from magnetic flux density measurement (Gao *et.al* [9]): In this study the researchers developed a new algorithm for MREIT based on radial basis function network and simplex method and tested the algorithm using a simulated human head phantom.
- Noise analysis in magnetic resonance electrical impedance tomography at 3 and 11 T field strengths (Sadleir *et.al* [10]): An expression for the standard deviation of measured magnetic flux density was derived and estimations are validated with experimental setup at two different field strengths. 10mA current pulses with a pulse width of 16msec injection were used. It is stated that the noise level in magnetic flux density is reduced as field strength is increased and the reduction factor is approximately proportional to the increase in the field strength.

- Basic setup for breast conductivity imaging using magnetic resonance electrical impedance tomography (Lee *et.al* [11]): In this study, researchers first simulated a 3D breast phantom and then carried out experiments with the corresponding phantom that contains saline and three polyacrylamide anomalies at 3T with 15mA (9 msec) injected current.
- Conductivity image reconstruction from defective data in MREIT: Numerical simulation and animal experiment (Lee et.al [12]): In this study, the researchers proposed a method for recovering magnetic flux data in defective regions based on physical properties and neighboring information. They used a sacrificed 10kg piglet in their experiments at 3T field strength. Current pulse amplitude and pulse width were 48mA and 30msec respectively. The corrected region was assumed to have uniform conductivity in their reconstruction.
- High field MREIT: setup and tissue phantom imaging at 11T (Sadleir et.al [13]): To be able to use lower current levels, the researchers used 11T magnet in their study. They used 5mA-20mA currents for 9msec-18msec and acquired images from agar and porcine muscle/turkey breast phantoms. They propose high-field MREIT as a research tool for obtaining accurate conductivity data from tissue samples and animal subjects.

As summarized above, most of the studies in literature aim to improve MREIT data acquisition techniques so that magnetic flux density can be measured with acceptable noise levels using MRI. No *in vivo* studies have been reported by other groups yet. This is due to the fact that current levels that other groups utilize are not safe for *in vivo* imaging. All studies suggest that MREIT have clinical potential (especially in breast cancer imaging) if low currents levels can be achieved.

BODY

In this multidisciplinary post-doctoral training grant, five specific aims were proposed.

Aim 1. Training stage: In order to be able to carry out the study proposed, principal investigator will receive training in tumor biology and DCE-MRI.

Aim 2. Development of 3D reconstruction algorithms for MREIT: In parallel with the training stage, new studies to improve the MREIT images will be carried out.

Aim 3. Test of 3D reconstruction using phantoms: Phantom experiments will be carried out for the 3D case.

Aim 4. Performing animal experiments using both techniques: Comparative animal experiments using ENU (N-Ethyl-N-Nitrosourea) induced malignant and benign breast tumors in rats will be carried out.

Aim 5. Statistical analysis: Efficacy of MREIT and comparison with DCE-MRI will be evaluated by ROC analysis of the acquired data and results from the pathological examination.

Statement of Work

The tasks to achieve the specific aims listed above are covered in the statement of work as outlined below. Items that had to be completed in the second year of the award period are indicated in bold.

Task 1. Acquire the necessary training in tumor biology and dynamic contrast-enhanced magnetic resonance imaging (Months 0-24)

a) Auditing courses and attending seminars on tumor biology (Months 0-12).
b) Training in DCE-MRI and preparation of animals for the training experiments (Months 13-16).
c) Experimental training in DCE-MRI (Months 17-21).
d) Statistical analysis of DCE-MRI data (Months 22-24).

Task 2. Implement a 3D-reconstruction algorithm for MREIT and test with simulations (Months 0-18).

a) 3D Mesh generation from MR slice images (Months 0-2).
b) Implementation of 3D FEM algorithm for arbitrary meshes (Months 3-6).

c) Implementation of the reconstruction algorithms and testing with simulation data (Months 6-10).
d) Incorporation of a priori anatomical information in image reconstruction (Months 11-12).
e) Determination of optimal electrode locations for arbitrary meshes (Months 13-14).
f) Making necessary updates in the algorithm (if necessary) by assessing the performance with the preliminary experimental results (Months 15-18).

Task 3. Modify existing hardware and pulse-sequences and test 3D reconstruction with phantoms and animals (Months 13-24).

a) Construction of 3D conductivity phantoms (Month 13).
b) Modifying and testing the pulse sequence for multi-slice imaging (Months 14-15).
c) Testing the system and adjusting the imaging parameters using phantoms (16-18).
d) Carrying out animal experiments using MREIT to determine the optimal parameters and electrode locations (Months 19-24).

Task 4. Perform animal experiments using both techniques.

a) Carrying out experiments on 50 ENU induced rats using both techniques for hypothesis testing. (Months 25-32).

Task 5. Receiver Operating Characteristics (ROC) analysis.

a) Analysis of MREIT and DCE-MRI data (Months 25-32).
b) Comparison with pathology results and ROC analysis (32-36).

Task 1. Training stage

For training in tumor biology and applications of different imaging modalities in breast cancer imaging, the principal investigator continued attending several seminars. One of the comments in the peer review panel summary was the lack of expansion of the training in tumor biology in other imaging modalities. This comment is taken into account in the selection of seminars to be attended.

Date	Presenter(s)	Title
May 16, 2005	Tae Suk Suh	Image-guided Applications in Medical Imaging and Radiation Therapy
May 19, 2005	Katherine W. Ferrara	New Developments in Ultrasound Imaging and Molecularly targeted Therapeutics
June 2, 2005	Nejat, K Egilmez	Cytokin-Encapsulated Microsphere Adjuvants for Cancer Immunotherapy
June 16, 2005	Robert J. Gillies	Imaging as a Biomarker in pre-clinical trials
October 27, 2005	Shiuan Chen	Breast Cancer Prevention/Treatment with Aromatase Inhibitors
December 15, 2005	Allison W. Kurian	Breast Cancer Screening in Women with High Inherited Risk: Emerging Strategies
January 9, 2006	David J. Yang	Techniques for Targeted Imaging Beyond FDG
January 19, 2006	Nola Hylton	MRI for Breast Cancer Staging and Assessment of Response to Preoperative Chemotherapy

Experimentation and analysis methods in dynamic contrast enhanced-magnetic resonance imaging (DCE-MRI) were also part of the training in the second year of the award. Principal investigator acquired training in data acquisition (adjustment of dynamic pulse sequences, synchronization with contrast agent injection) and performed experiments herself that will be crucial in the next year of the project where 50 animals are going to be scanned. For the data analysis, the programs developed in UCI Center for Functional Onco-Imaging based on estimating kinetic parameters outlined by Tofts *et.al* [14] were used.

Task 2 (e-f)

In the second year, one of the tasks to be completed was determination of optimal electrode locations and update of the reconstruction algorithm using the preliminary experimental results. For this purpose, we carried out extensive phantom experiments with low amplitude currents, developed methods to handle the data that is contaminated with acquisition noise, and investigated contrast and spatial resolution limits at these current levels. Note that the improved data acquisition method (with revised pulse sequence and hardware) that is explained in the next section is an important part of the improvement in the reconstruction.

As explained in the introduction section, measurement of magnetic flux density with acceptable noise levels using low amplitude currents is extremely important to be able to translate the technique to *in vivo* animal and ultimately to clinical studies. For this purpose we limited our current level to a safety level of 1mA and carried out experiments using spatial and contrast resolution phantoms [C1, J2]. In order to understand the spatial resolution for low amplitude currents, phantoms that contain objects with different diameters (3 mm, 5 mm, and 8 mm) and extreme conductivity cases (insulator (-ins) and high conductivity (-cond)) were reconstructed. For the insulator cases, hollow cylinders filled with the same agarose-NaCl solution as the background were used. For the high conductivity cases, a solution with 10 gr NaCl/100 gr water, which gives a 6.70:1 contrast with respect to background, was used. The results for spatial resolution analysis are summarized in Table 2 in [J2]. To evaluate the system performance at different contrast levels, 15mm-diameter objects with five different conductivity values between the two extreme cases used in the spatial resolution analysis were selected. The true conductivity and ratio values and reconstructed peak object and mean background values are summarized in Table 3 in [J3]. Comparison of our results with literature suggests that sensitivity matrix based reconstruction is less susceptible to noise in measurements compared to gradient-based algorithms. It is possible reconstruct conductivity images with 3mm resolution even using 1mA current.

Our reconstruction algorithm utilizes numerical calculation of the magnetic flux density for a given initial conductivity distribution using the boundary conditions (i.e. electrode positions and current) applied to the real object. The magnetic flux density has high variation near the electrodes and any misalignment in the electrode positions created artifacts in the reconstructed image. We investigated various correction algorithms to reduce these artifacts. Three electrode misalignment correction algorithms proposed are: MASK, SHIFT, and REG. These algorithms and results are summarized in [C3] given in the appendix. Each of the algorithms improves reconstruction, with the best results occurring when all three methods are applied.

One other task was the determination of the optimal current injection schemes. It is theoretically shown that at least two current injection distributions satisfying $|\mathbf{J}_1(x,y) \times \mathbf{J}_2(x,y)|$ must be used for unique reconstruction [15]. We tried different electrode locations and observed that placing four electrode around the periphery at angles $\{\pi/4, 3\pi/4, 5\pi/4, 7\pi/4\}$ gives the optimal coverage. After the locations were determined, next step is determination of the electrode pairs to be used. Opposite electrode pairs provide the most region coverage considering the current distribution inside the object, however, may fail to detect regions close to the boundary between electrodes. In order to handle these situations, we investigated multiple current injection schemes in MREIT [C4]. We have shown that selection of the current injection schemes to be used requires balancing overall contrast with improved spatial resolution in the periphery regions, and will thus depend on the object to be imaged and the desired information. One other criteria in choosing number of current injection schemes is the total data acquisition time. Therefore, it is desirable to get more coverage with two current injection cases (which is the theoretical minimum). In MREIT, although only the phase MR images are used for conductivity reconstruction, magnitude images are simultaneously reconstructed providing a priori anatomical information for

MREIT. In our animal experiments, we used MR anatomical image to verify that the region of interest is adequately probed. Animal image reconstruction results are covered in the next section.

We also investigated the possible use of MREIT for dynamic imaging. Previous MREIT studies have focused on static imaging, whereas detecting changes in conductivity over time could provide additional diagnostic information. An ion diffusion phantom is created to simulate conductivity variation in time and the change is monitored using sub-milliamp injected currents. The results are presented in [C2].

Task 3. Modification of existing hardware and pulse-sequences and test 3D reconstruction with phantoms and animals

3D phantom are constructed using agar-NaCl solutions with different conductivity values and some acrylic components (Task3a). An acrylic cylinder with 7cm diameter and 10 cm height is used as the base mold and filled with desired background coductivity. To create different distrubutions, we using cylinder and spherical components to create openings to be filled with different solutions. The major difference between the 2D and 3D phantom is the placement of the electrodes. In 2D case, 5mm thick electrodes were placed all along the z-axis of the phantom (10mm) to achieve uniform current distrubution in different planes whereas in 3D we used electrodes with 5mmx5mm size at the center height and this is acounted in the 3D finite element solver.

In order to be able to measure magnetic flux density at low amplitude currents, we implemented various modifications in our hardware and pulse sequence (Task 3b) and carried out various phantom experiments for optimization (Task3c). In our earlier studies, we were using sine wave current synchronized with the first RF pulse in a conventional spin echo sequence [J3]. In this scheme, the pulse sequence was triggering an external function generator to output a burst sine wave, making it more susceptible to small timing errors. In the new scheme, instead of using sine wave we used a train of pulses [J1, J2] where pulse sequence directly controls polarity and timing of each pulse sequence, which provides more accurate synchronization. Another modification in the pulse sequence is that no current is applied during RF refocusing pulses. In older sequence, RF pulses were applied during application of the burst sine wave and it was suspected that the small currents during application of RF pulses were leading slight shifts in the slice selection location. We also maintained slice selection gradient for refocusing pulses throughout the current application. This functions as crusher gradient, dephasing unwanted secondary/stimulated echoes generated from multiple RF pulses. Without larger crushers, resulting images exhibited significant interference patterns. Our original sequence collected single slice images only, therefore, we extended the base sequence for multi-slice acquisition for 3D data collection. We tested various T_E values and number of cycles of injected current to determine optimum SNR. Optimum T_E is found at T_2 value of imaged object, which is consistent with findings in the literature [16].

In addition to these modifications in the pulse sequence, we also constructed an upgraded current source/multiplexer circuit. In the new current source, selection of the injection profile and pulse polarity is controlled by the pulse sequence, allowing more precise timing and synchronization.

All these modifications were essential to be able to carry out *in vivo* animal experiments planned in Task 3d. After testing our new system with phantom studies, we performed experiments using tumor bearing rats. These tumors were either induced by the carcinogen ENU or R3230 AC tumor grafts. For animal imaging, a special animal holder was prepared from acrylic sheets. In this holder electrodes were placed on acrylic hollow tubes filled with $CuSO_4$ solution mark the electrode positions precisely in the images. The precise localization of electrode positions is critical for accurate assignment of boundary conditions and thus, effects the reconstruction performance. Current carrying wires ran along these tubes, which were in z-direction. This is essential to minimize interference from the magnetic fields generated by current in the wires. The animal was anesthetized by injection of ketamine and xylazine and placed

inside the holder. The skin areas of contact were shaved to guarantee good contact. An anatomical image was collected using FSE sequence prior to the MREIT images. A single slice with 6*mm* thickness was collected from the same anatomical location as the MREIT image. The data matrix was 256 × 256, FOV = 10cm, T_R = 4sec, T_E = 40msec, and NEX = 4 (signal averages). MREIT images were collected using the pulse sequence in [J3] with T_R = 500mses, T_E = 30msec, NEX = 8, 64 × 64 data matrix, field of view, FOV = 10cm, 6mm slice thickness, with an AC current of 1mA peak, 100Hz and 4 cycles. Reconstructed images from six animals are shown in Fig. 1.

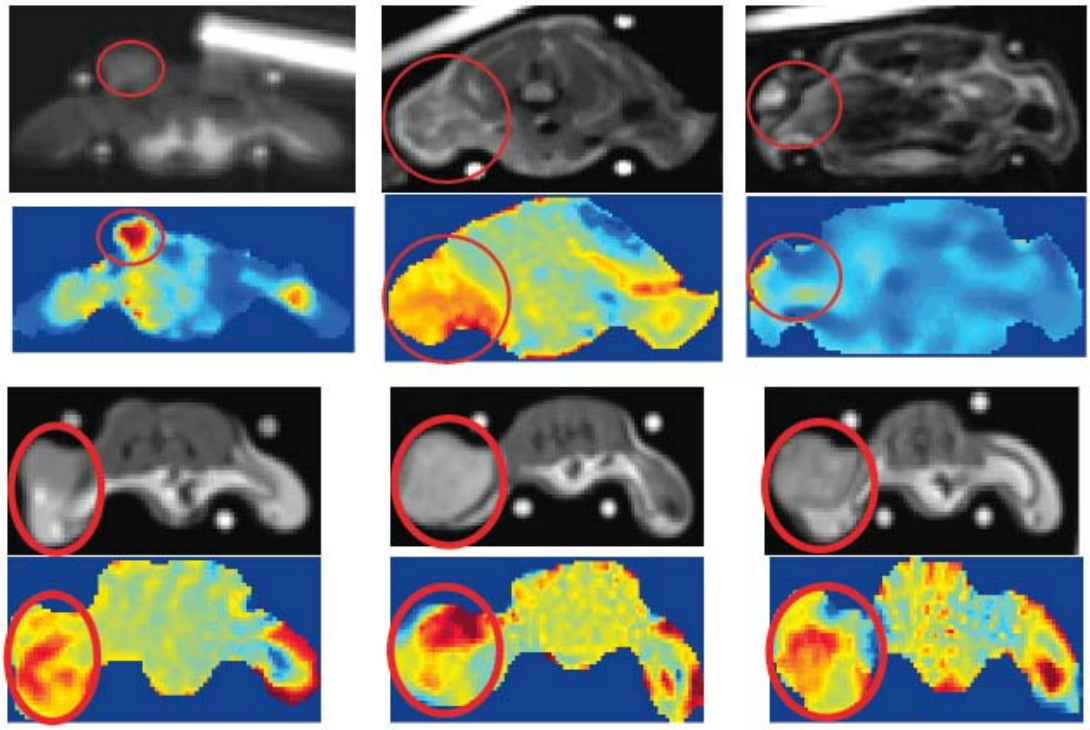

Fig 1. Anatomical MR and corresponding conductivity images for six different animals.

In each image pair, top image shows the anatomical MR image and bottom image shows the corresponding conductivity image. Circled areas show the tumor location. For each animal, region of interests were selected over the tumor region and over the rest of the body. Since these images provide only relative conductivity measures, the ratio of mean conductivity in the tumor divided by the mean conductivity in normal tissue was calculated for each animal. The mean of these ratios across all animals was μ= 2.26, σ= 0.62. In other words, the mean conductivity was, on the average, 2.26 times higher than the conductivity in normal regions.

The major challenge we encountered in animal experiments was the errors in the magnetic flux density measurements due to motion artifacts. The motion artifact in the MR image is clearly seen in top left image pair in Fig 1. For some cases, this effect was worse and the data had to be discarded. We are now working on a faster imaging sequence that will be less susceptible to motion.

References

[1] A. J. Surowiec, S. S. Stuchly, J. R. Barr, and A. Swarup, "Dielectric Properties of Breast Carcinoma and the Surrounding Tissues," *IEEE Trans. on BME*, vol.35, no. 4, pp. 257- 263, 1988.

[2] A. Malich, T. Boehm, M. Facius, M. G. Freesmeyer, M. Fleck, R. Anderson, and W. A. Kaiser, "Differentiation of Mammographically Suspicious Lesions: Evaluation of Breast Ultrasound, MRI Mammography and Electrical Impedance Scanning as Adjunctive Technologies in Breast Cancer

Detection," *Clinical Radiology*, vol. 56, pp. 278-283, 2001.

[3] O. Birgul, B. M. Eyuboglu, and Y. Z. Ider, "Current constrained voltage scaled reconstruction (CCVSR) algorithm for MREIT and its performance with different probing current patterns," *Physics in Medicine and Biology*, vol. 48, no.5, pp. 653-671, 2003.

[4] O. Birgul, B. M. Eyuboglu, and Y. Z. Ider, "Experimental results for 2D magnetic resonance electrical impedance tomography (MREIT) using magnetic flux density in one direction," *Physics in Medicine and Biology*, vol. 48, No.21, pp. 3485-3504, 2003.

[5] L. T. Muftuler, M. J. Hamamura, O. Birgul, and O. Nalcioglu, "Resolution and Contrast in Magnetic Resonance Electrical Impedance Tomography (MREIT) and Its Application to Cancer Imaging, " T*echnology in Cancer Research and Treatment*, vol. 3, no. 6, pp. 599-609, 2004.

[6] M. Y. Su, A. Muhler, X. Lao, and O. Nalcioglu, "Tumor Characterization with Dynamic Contrast-Enhanced MRI Using MR Contrast Agents of Various Molecular Weights," *Magnetic Resonance in Medicine*, vol. 39, pp. 259-269, 1998.

[7] M. Y. Su, Z. Wang, P. M. Carpenter, X. Lao, A. Muhler, and O. Nalcioglu, "Characterization of N-Ethyl-N-Nitrosourea-Induced Malignant and Benign Breast Tumors in Rats by Using Three MR Contrast Agents," *Journal of Magnetic Resonance Imaging*, vol. 9, pp. 177-186, 1999.

[8] S. H. Oh, B. I. Lee, E. J. Woo, S. Y. Lee, T. S. Kim, O. Kwon and J. K. Seo, "Electrical conductivity images of biological tissue phantoms in MREIT," *Physiological Measurement*, vol. 26, pp. S279-288, 2005.

[9] N. Gao, S. A. Zhu, and B. He, "Estimation of electrical conductivity distribution within the human head from magnetic flux density measurement," *Physics in Medicine and Biology*, vol. 50, pp. 2675-2687, 2005.

[10] R. Sadleir, S. Grant, S. U. Zhang, B. I. Lee, H. C. Pyo, S. H. Oh, C. Park, E. J. Woo, S. Y. Lee, O. Kwon, and J. K. Seo, "Noise analysis in magnetic resonance electrical impedance tomography at 3 and 11T field strengths," *Physiological Measurement*, vol. 26, pp. 875-884, 2005.

[11] B. I. Lee, S. H. Oh, T. S. Kim, E. J. Woo, O. Kwon, and J. K. Seo, "Basic Setup for Breast Conductivity Imaging using Magnetic Resonance Electrical Impedance Tomography," *Physics in Medicine and Biology*, vol. 51, pp. 443-455, 2006.

[12] S. H. Lee, J. K. Seo, C. Park, B. I. Lee, E. J. Woo, S. Y. Lee, O. Kwon, and J. Hahn, "Conductivity Image Reconstruction From Defective Data in MREIT: Numerical Simulation and Animal Experiment, " *IEEE Transactions on Medical Imaging*, vol. 25, no. 2, pp 168-176, 2006.

[13] R. Sadleir, S. Grant, S. U. Zhang, S. H. Oh, B. I. Lee, and E. J. Woong, "High field MREIT setup and tissue phantom imaging at 11T," Physiological Measurement, vol. 27, pp. S261-270, 2006.

[14] P. S. Tofts, G. Brix, D. L. Buckley, J. L. Evelhoch, E. Henderson, M. V. Knopp, H. B. W. Larsson, T. Y. Lee, N. A. Mayr, G. J. M. Parker, R. E. Port, J. Taylor, and R. M. Weisskoff, "Estimating Kinetic Parameters from Dynamic Contrast-Enhance T1-Weighted MRI of a Diffusable Tracer: Standardized Quantities and Symbols," *Journal of Magnetic Resonance Imaging*. vol. 10, pp. 223-232, 1999.

[15] O. Kwon, E. J. Woo, J. R. Yoon, and J. K. Seo, "Magnetic Resonance Electrical Impedance Tomography (MREIT): Simulation Study of J-Substitution Algorithm, " IEEE Transactions on Biomedical Engineering, vol. 49, no. 2, pp 160-167, 2002.

[16] G. C. Scott, M. L. G. Joy, R. L. Armstrong, and R. M Hankelman, "Measurement of Non-uniform Current Density by Magnetic Resonance," *IEEE Trans on Medical Imaging*, vol. 10, pp. 362-374, 1991.

REPORTABLE OUTCOMES

Journal Papers

[J1] Hamamura M J, Muftuler T M, **Birgul O**, and Nalcioglu O, "Measurement of ion diffusion using magnetic resonance electrical imaging tomography," *Physics in Medicine and Biology*, vol 51, pp 2753-2762.

[J2] **Birgul O**, Hamamura M J, Muftuler T M, and Nalcioglu O, "Contrast and spatial resolution in MREIT using low amplitude currents," *submitted to Physics in Medicine and Biology*, (accepted with revisions).

[J3] Muftuler T, Hamamura M J, **Birgul O**, and Nalcioglu O, "In vivo MRI Electrical Impedance Tomography (MREIT) of Tumors," *submitted to Technology in Cancer Research and Treatment, Special issue on multi-modality imaging* (in review).

Invited Talks

[I1] **Birgul O**, Hamamura M J, Muftuler L T, and Nalcioglu O, "Magnetic Resonance-Electrical Impedance Tomography in Breast Cancer Imaging," *IEEE, International Symposium on Biomedical Imaging*, Arlington VI, 2006.

Conference Papers

[C1] **Birgul O**, Muftuler L T, Hamamura M J, and Nalcioglu O, "Reconstruction of Irregular Conductivity Distributions using MREIT at Low Current Levels," *ISMRM 14th Scientific Meeting and Exhibition Seattle, Washington*, May 2006.

[C2] Hamamura M J, Muftuler L T, **Birgul O**, and Nalcioglu O, "Dynamic Magnetic Resonance Electrical Impedance Tomography Using Sub-Milliamp Injected Currents," *ISMRM 14th Scientific Meeting and Exhibition Seattle, Washington*, May 2006.

[C3] Hamamura M J, Muftuler L T, **Birgul O**, and Nalcioglu O, "Electrode Misalignment Correction Algorithms In Magnetic Resonance Electrical Impedance Tomography," *ISMRM 14th Scientific Meeting and Exhibition Seattle, Washington*, May 2006.

[C4] Hamamura M J, Muftuler L T, **Birgul O**, and Nalcioglu O, "Multiple Current Injection Schemes In Magnetic Resonance Electrical Impedance Tomography," *ISMRM 14th Scientific Meeting and Exhibition Seattle, Washington*, May 2006.

[C5] Muftuler L T, Hamamura M J, **Birgul O**, and Nalcioglu O, "In Vivo MRI Based Electrical Impedance Tomography of Malignant Tumors," *ISMRM 14th Scientific Meeting and Exhibition Seattle, Washington*, May 2006.

Conference Abstracts and Posters

[P1] **Birgul O**, Muftuler L T, Hamamura M J, and Nalcioglu O" Magnetic Resonance - Electrical Impedance Tomography (MREIT) Using Iterated Sensitivity Reconstruction Algorithm," IEEE AIPR 2005 Workshop, Multi-modal Imaging Session, Washington, DC, October 19-21, 2005.

[P2] **Birgul O**, Muftuler L T, Hamamura M, and Nalcioglu O, "Iterated Sensitivity Algorithm for Magnetic Resonance Electrical Impedance Tomography," *Era of Hope DOD Breast Cancer Research Program Meeting*, Philadelphia PA, June 8-11, 2005.

[P3] Muftuler L T, Hamamura M, **Birgul O**, and Nalcioglu O, "MRI Based Electrical Impedance Imaging of Tumors," *Era of Hope DOD Breast Cancer Research Program Meeting*, Philadelphia PA, June 8-11, 2005.

(Journal and conference papers are included in the appendix section)

KEY RESEARCH ACCOMPLISHMENTS

- Training of the principal investigator in DCE-MRI.
- Development of 3D imaging sequence.
- Modification and testing the hardware and the pulse sequence using low amplitude currents suitable for small animal experiments.
- Preliminary animal experiments and reconstruction.

CONCLUSIONS

In the second year of the award period, the specific aims were further training of the PI in breast cancer and DCE-MRI data acquisition/processing and implementation and improvement of hardware-pulse sequences that are required in animal experiments. Major challenges were measuring magnetic flux density with acceptable noise at safe current levels and error in the measured field due to motion artifacts. With appropriate modifications in our hardware and optimization of the pulse sequences, we can safely measure magnetic flux density from small animals at 1mA current level. We are now developing a new pulse sequence using our experience for faster data acquistion that will be less effected by the motion artifacts.

Next steps in the study will be:

- Performing animal experiments using both techniques on 50 animals.
- Statistical analysis of MREIT and DCE-MRI data.
- Comparison of our results with pathology results.

APPENDICES

Reprints of the documents listed in reportable outcomes section.

INSTITUTE OF PHYSICS PUBLISHING PHYSICS IN MEDICINE AND BIOLOGY

Phys. Med. Biol. **51** (2006) 2753–2762 doi:10.1088/0031-9155/51/11/005

Measurement of ion diffusion using magnetic resonance electrical impedance tomography

Mark J Hamamura, L Tugan Muftuler, Ozlem Birgul and Orhan Nalcioglu

Tu & Yuen Center for Functional Onco-Imaging, University of California, 164 Irvine Hall, Irvine, CA 92697-5020, USA

E-mail: markjham@uci.edu

Received 9 February 2006, in final form 10 February 2006
Published 9 May 2006
Online at stacks.iop.org/PMB/51/2753

Abstract

In magnetic resonance electrical impedance tomography (MREIT), currents are applied to an object, the resulting magnetic flux density measured using MRI and the conductivity distribution reconstructed using these MRI data. In this study, we assess the ability of MREIT to monitor changes in the conductivity distribution of an agarose gel phantom, using injected current pulses of 900 μA. The phantom initially contained a distinct region of high sodium chloride concentration which diffused into the background over time. MREIT data were collected over a 12 h span, and conductivity images were reconstructed using the iterative sensitivity matrix method with Tikhonov regularization. The results indicate that MREIT was able to monitor the changing conductivity and concentration distributions resulting from the diffusion of ions within the agarose gel phantom.

(Some figures in this article are in colour only in the electronic version)

1. Introduction

In vitro studies have shown that the electrical conductivity of malignancies may be 20 to 40 times higher than healthy tissues and benign formations (Surowiec *et al* 1988, Jossinet 1998). Therefore, *in vivo* conductivity imaging could aid in the diagnosis and characterization of suspicious lesions. Electrical impedance tomography (EIT) is a conductivity imaging modality that consists of three general steps. A current distribution is established within the object of interest, the effects of these currents are measured, and then these measurement data are used to reconstruct the conductivity distribution within the object. In conventional EIT, surface electrodes are used to inject current into the object and to acquire voltage measurements. This technique is constrained by the physically limited number of measurement electrodes and restriction to surface measurements. As a result, it suffers from poor, non-uniform spatial

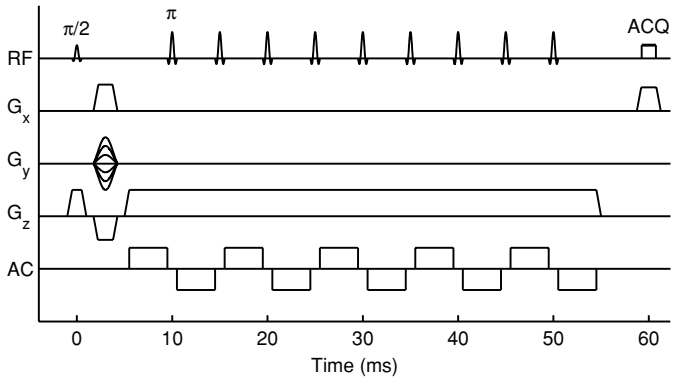

Figure 1. MREIT pulse sequence diagram.

resolution and low sensitivity of the voltages to conductivity changes in the interior regions (Seagar *et al* 1987).

In magnetic resonance electrical impedance tomography (MREIT), MRI is used to measure the effects of applied currents throughout the entire object. These applied currents generate a magnetic flux density, of which the component parallel to the main static field can be measured using an appropriate pulse sequence (Scott *et al* 1991, Ider and Muftuler 1997, Mikac *et al* 2001). Given this single component of current-generated magnetic flux density, several algorithms have been proposed to reconstruct the conductivity distribution. These include the sensitivity matrix method (Ider and Birgul 1998, Birgul *et al* 2003b), $\nabla^2 B_z$ algorithms (Seo *et al* 2003, Ider and Onart 2004) and ∇B_z algorithms (Park *et al* 2004a, 2004b). Several MREIT studies using biological tissue phantoms have been reported (Khang *et al* 2002, Lee *et al* 2003, Oh *et al* 2005). However, these studies focused on reconstructing static conductivity distributions using injected current levels of at least 12 mA. The ability to monitor changes in conductivity over time could provide additional diagnostic information, such as in monitoring tumour growth and treatment. In this study, we assessed the ability of MREIT to monitor changes in conductivity over time using sub-milliamp injected currents more appropriate for human use. Validating this ability is a necessary step towards the imaging and monitoring of human subjects using MREIT.

2. Methods

2.1. Theory

In MREIT, applied currents establish a conductivity-dependent current density distribution within an object, which in turn generates a magnetic flux density according to Ampere's Law. Thus, magnetic flux density measurements contain information about the conductivity distribution. In this study, current pulses of alternating polarity were applied to a test phantom using surface electrodes. For alternating currents, the component of magnetic flux density parallel to the main static field (z-component) can be measured by MRI using a modified spin-echo sequence (Mikac *et al* 2001). The pulse sequence used in this study is shown in figure 1. The current-generated magnetic flux density introduces a phase shift φ in the MR image, given as:

$$\varphi(\mathbf{r}) = 2\gamma N T_{\text{pulse}} B(\mathbf{r}) \tag{1}$$

where γ is the gyromagnetic ratio, N is the number of cycles of injected current such that each cycle consists of one positive and one negative pulse, T_{pulse} is the duration of each pulse, and $B(\mathbf{r})$ is the amplitude of z-component current-generated magnetic flux density at point $\mathbf{r}$. Measurement of this phase shift allows for calculation of $B(\mathbf{r})$.

For a given set of electrodes used for current injection, data were collected twice, each with opposite polarities in the applied current pulses. The resulting phase maps were subtracted then divided by two, so as to cancel out any additional phase contributions, such as those arising from small imperfections in the hardware timing. A given set of injecting electrodes forms an 'injection profile'. Data from at least two different injection profiles are required to reconstruct a unique solution (Kwon *et al* 2002). Previous MREIT studies have shown that using just two profiles is sufficient for reconstructing accurate images. This is a significant advantage over conventional EIT, which typically requires the use of several (16 or more) electrodes.

For reconstructing the conductivity distribution from the z-component magnetic flux density data, this study utilized the sensitivity matrix method (SMM). The object domain was discretized into a mesh of first-order triangular elements, chosen for compatibility with the finite element method (Reddy 1993). A linear relationship between conductivity perturbations and z-component magnetic flux density perturbations was then assumed, such that:

$$\Delta B_z = \mathbf{S}\Delta\sigma \tag{2}$$

where $\mathbf{S}$ is known as the 'sensitivity' matrix. Given m measurement points and n conductivity elements, ΔB_z is an $m \times 1$ vector, $\Delta\sigma$ is an $n \times 1$ vector, $\mathbf{S}$ is an $m \times n$ matrix, and the matrix element S_{ij} is the change in the ith magnetic flux density measurement due to a small variation in the conductivity of the jth element. An initial conductivity distribution σ_{initial} was assumed (e.g. uniform conductivity), and the problem linearized around this initial condition:

$$B_{\text{final}} - B_{\text{initial}} = \mathbf{S}(\sigma_{\text{final}} - \sigma_{\text{initial}}) \tag{3}$$

where B_{initial} is the z-component magnetic flux density distribution given σ_{initial} and calculated using the finite element method and Biot-Savart law, B_{final} is the MRI measured z-component magnetic flux density, σ_{final} is the actual (unknown) conductivity distribution, and $\mathbf{S}$ is the sensitivity matrix such that:

$$S_{ij} = \left[\frac{\partial B_i}{\partial \sigma_j}\right]_{\sigma=\sigma_{\text{initial}}}. \tag{4}$$

In general, $\mathbf{S}$ is an ill-conditioned matrix, so that a simple least-squares fit cannot be used to solve for σ_{final}. In this study, the linear equation was solved using the conjugate gradient method with Tikhonov regularization, where σ_{final} was found by:

$$\min_{\sigma_{\text{final}}}\{\|\mathbf{S}\Delta\sigma - \Delta B_z\|^2 + \lambda\|\Delta\sigma\|^2\} \tag{5}$$

where λ is a regularization parameter (Golub *et al* 1999). The regularization parameter λ was chosen such that the calculated z-component magnetic flux density generated by the reconstructed conductivity distribution was closest to the MRI-measured magnetic flux density.

$$\min_{\lambda}\{\|B_{\text{final}} - [B(\sigma)]_{\sigma=\sigma_{\text{final}}(\lambda)}\|\}. \tag{6}$$

After finding σ_{final}, if the change in conductivity $\Delta\sigma$ was greater than some predefined threshold, then this σ_{final} was assigned as the new, updated σ_{initial}, and the process was iterated.

The SMM reconstructs relative conductivities. Thus, the true conductivity distribution σ_{true} is related to the reconstructed conductivity distribution σ_{final} by a constant scaling factor K:

$$\sigma_{\text{true}} = K\sigma_{\text{final}}. \tag{7}$$

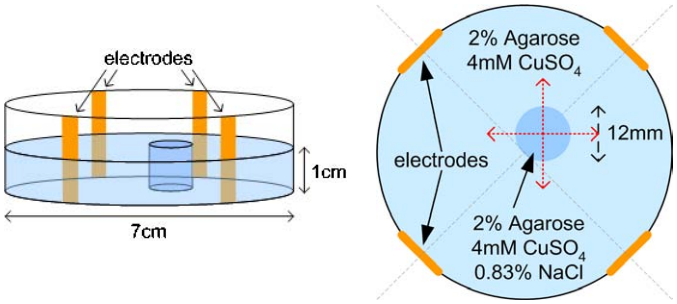

Figure 2. (a) Side view and (b) top view of the phantom used to monitor the diffusion of NaCl.

Determining the absolute conductivity distribution requires an additional constraint, such as a surface voltage measurement (Birgul *et al* 2003a).

2.2. Phantom

The previously outlined methods were used to monitor the conductivity distribution within an agarose gel phantom. The conductivities of several 4 mM $CuSO_4$ and 2% agarose mixtures with a range of NaCl concentrations from 0% to 1% were measured using the 4-electrode method (Baumann *et al* 1997). Within this range, a linear relationship was found:

$$\sigma = AC + E \tag{8}$$

where the conductivity σ is in units of S m^{-1}, the NaCl concentration C is in units of g/100 ml water, and the constants A and E are 1.7 and 0.074 respectively. For larger NaCl concentrations, the relationship becomes nonlinear (Fuoss and Onsanger 1957).

For the phantom, a hollow acrylic disc with an inner diameter of 7 cm was filled to a thickness of 1 cm with 4 mM $CuSO_4$ and 2% (g/100 ml water) agarose. Within this disc, a smaller cylindrical region of 12 mm diameter and 1 cm thickness was filled with 4 mM $CuSO_4$, 2% agarose and 0.83% NaCl. This NaCl concentration was selected using (8) to provide a conductivity contrast of 20 relative to the background. An actual conductivity contrast of 19.7 was found by measuring the prepared gels using the 4-electrode method. The initial mixtures within each of these two regions were assumed to be homogeneous. The phantom was constructed such that within the phantom, the overall concentration distribution did not vary along the z-direction. A schematic of the phantom is shown in figure 2.

To measure the conductivity distribution within the phantom using MREIT, four copper electrodes each 6.35 mm wide were placed equidistant along the inner wall of the acrylic disc and used to inject currents into the interior region (figure 2). Using (7) and (8), measurement of the conductivity distribution was used to map the NaCl concentration distribution. The scaling factor K was determined by applying the constraint that the total amount of NaCl in the phantom remained constant:

$$\int_{\text{phantom}} C \, \mathrm{d}v = \text{constant}. \tag{9}$$

Measurements of the conductivity distribution over time were used to monitor the diffusion process occurring within the phantom.

In the phantom's initial state, there existed a distinct region containing NaCl and a background containing no NaCl. Over time, the NaCl diffused from the region of higher concentration to the region of lower concentration as governed by the diffusion equation:

$$\frac{\partial C}{\partial t} = \nabla \cdot D\nabla C \tag{10}$$

where C is the concentration of the diffusing substance and D is the diffusion constant. Due to the geometry of the phantom, there existed no concentration gradient along the z-direction within the phantom. Thus this diffusion process was independent of the z-direction and can be analysed in 2D. For a disc of radius a on an infinite place surface, the concentration C at radius r and time t is given as:

$$C(r) = \frac{C_i}{2Dt} \exp\left(\frac{-r^2}{4Dt}\right) \int_0^a \exp\left(\frac{-r'^2}{4Dt}\right) I_0\left(\frac{rr'}{2Dt}\right) r' \, \mathrm{d}r' \tag{11}$$

where C_i is the initial uniform concentration of the disc and I_0 is the modified Bessel function of the first kind of order zero (Crank 1975). For a given time $t > 0$, the peak concentration C is located at the centre of the disc, and is given as

$$C = C_i \left(1 - \exp\left(\frac{-a^2}{4Dt}\right)\right). \tag{12}$$

2.3. Experiment

The agarose gel phantom was placed within a 4T MRI scanner with the plane of the disc aligned perpendicular to the main static field. Currents within the phantom were constrained within this plane and the current density distribution contained a negligible z-component. As a result, the current-generated magnetic flux density within the phantom was primarily along the main static field axis. This was ideal since the pulse sequence only detects the z-component of any magnetic flux density. Currents were delivered to the electrodes using thin copper wires. These wires were aligned parallel to the main static field for up to 10 cm away from the phantom, such that the magnetic flux density they generated contained a negligible z-component in the phantom, and thus did not affect the MRI measurements. A current-source circuit was constructed and used to generate the injected currents (Baumann *et al* 1997). Synchronization of the circuit output with the pulse sequence was controlled by the scanner computer through a digital interface.

An MREIT measurement was acquired as soon as possible after preparation of the agarose gel phantom (30 min). Additional measurements were taken at 1 h intervals after phantom preparation for up to 8 h, followed by scans at 10 and 12 h. For each time point, data were collected for two injection profiles, using pairs of electrodes directly opposite of each other (figure 4). Both data sets were used simultaneously in the conductivity reconstruction algorithms. For each injection profile, data were collected using the previously outlined pulse sequence, injecting 5 cycles of current with an amplitude of 900 μA, a pulse length of 3567 μs and a cycle period of 10 ms (figure 1). Other scan parameters were: TR = 500 ms, TE = 60 ms, slice thickness = 5 mm, FOV = 100 mm, matrix = 64 × 64, NEX = 8. Raw MRI data were exported to a separate computer for processing. Magnetic flux density calculations and reconstruction algorithms utilizing the iterative SMM with Tikhonov regularization were developed using MATLAB. For reconstruction, a circular finite element mesh with 1089 nodes and 2048 triangular elements was utilized, as shown in figure 3(a). For each timepoint, the reconstruction was iterated until successive iterations resulted in not more than a 1% change in the peak conductivity value.

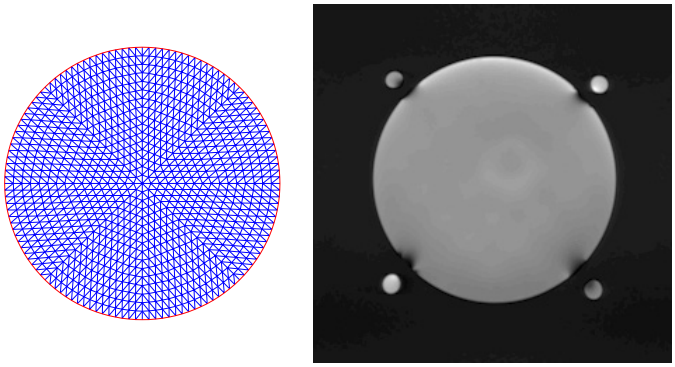

(a) (b)

Figure 3. (a) Finite element mesh used for reconstruction. (b) Spin echo image of the phantom. The smaller circular markers around the periphery were used to locate the electrodes during reconstruction.

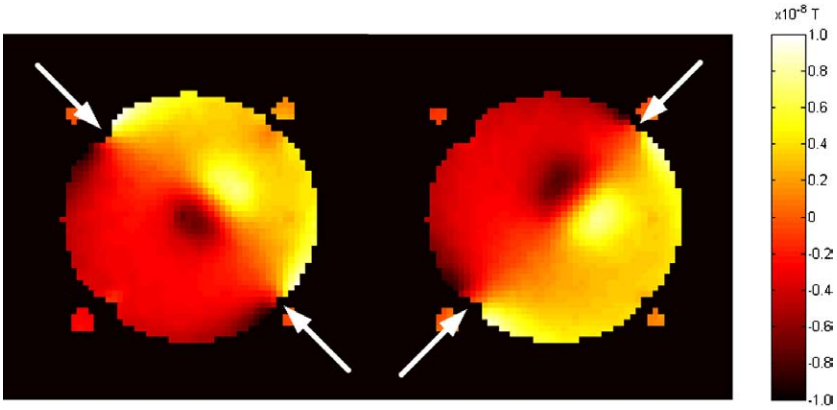

Figure 4. Reconstructed z-component magnetic flux density distributions at the first time point for the two injection profiles. The white arrows indicate the location of the current injecting electrodes.

3. Results

Figure 3(b) shows the MR magnitude image of the phantom taken using a standard spin-echo sequence just after at the first time point. The scan parameters were: TR = 1 s, TE = 20 ms, slice thickness = 5 mm, FOV = 100 mm, matrix = 256 × 256, NEX = 2. Despite two distinct regions of different NaCl concentrations, there is little contrast in this image.

Figure 4 shows the calculated z-component magnetic flux density at the first time point for the two injection profiles. Figure 5 shows the reconstructed conductivity images, obtained by processing the magnetic flux density data with the iterative SMM with Tikhonov regularization. Unlike the MR magnitude image, these conductivity images show a clear contrast between regions of different NaCl concentrations. For each time point, the spatial profile centred on the initial high NaCl concentration region was calculated by averaging the radial profiles taken along four different directions as shown by the red dotted lines in figure 2(b). The resulting curves are plotted in figure 6. Over time, the higher conductivity region broadened

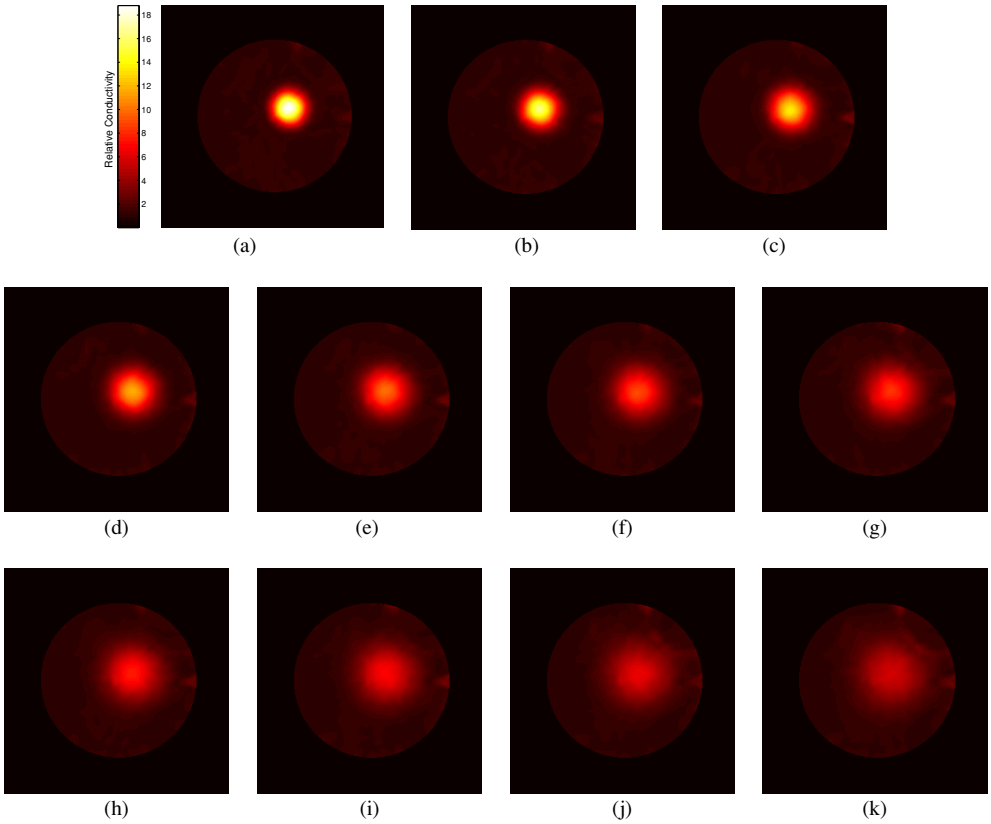

Figure 5. Reconstructed conductivity distribution (a) 30 min, (b) 1 h, (c) 2 h, (d) 3 h, (e) 4 h, (f) 5 h, (g) 6 h, (h) 7 h, (i) 8 h, (j) 10 h and (k) 12 h after phantom preparation.

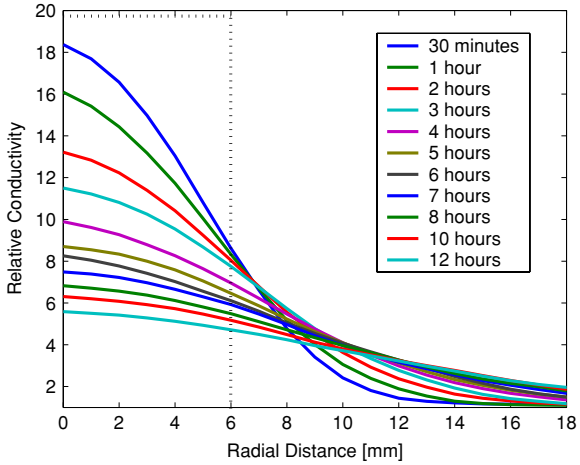

Figure 6. Comparison of the spatial profiles of the inner disc. The initial profile at $t = 0$ is denoted by the dotted line.

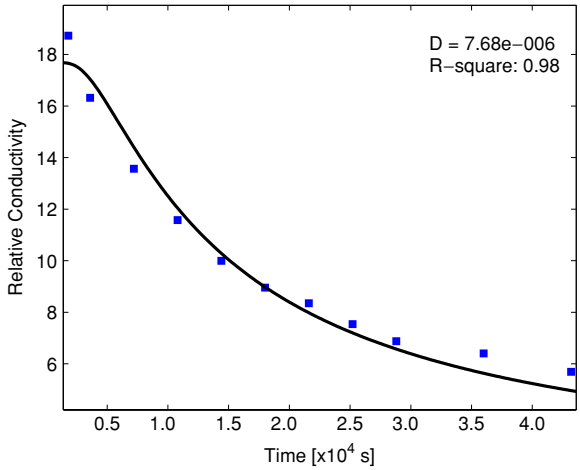

Figure 7. Decay of the peak conductivity. Reconstructed values denoted by the blue squares were fitted to (12) resulting in the black curve.

and decreased in magnitude, and the border between initial regions became less distinct. The change in the conductivity distribution is consistent with the diffusion of NaCl from the initial disc region into the background.

To quantify this diffusion, the peak conductivity value for each time point was scaled using (9) then fitted to (12) using the Curve Fitting Toolbox of MATLAB. The results are shown in figure 7. The peak values appear to coincide with the theoretical curve, indicating that the changing reconstructed conductivity distributions over time can be attributed to the diffusion process. An experimental diffusion constant of $D = 7.68 \times 10^{-6}$ cm^2 s^{-1} was obtained.

4. Discussion

The previous results indicate that MREIT was able to monitor the changing conductivity distribution resulting from the diffusion of ions within the agarose gel phantom. The experimentally determined diffusion constant is 45% smaller than the previously reported measurement of 1.4×10^{-5} cm^2 s^{-1} by Schantz and Lauffer (1962). However, their study investigated NaCl in an estimated 1.5% agarose gel, which can in part explain their faster diffusion. The smaller diffusion constant for the MREIT phantom can also be attributed to its finite shape and confined volume. Equation (11) assumes that diffusion occurs on an infinite plane. In a restricted area, NaCl can accumulate, which decreases the apparent rate of diffusion.

In using the SMM, only relative changes in conductivity can be found. However, in monitoring the phantom, only contrasts in conductivity were required to observe the ion diffusion. In applications such as tumour characterization, differences in conductivity between suspicious lesions and surrounding background tissue may be more significant than absolute conductivity values.

While data were collected every hour, shorter time resolutions are possible and limited by the rate at which data can be acquired. For the scan parameters used in this study, data for one injection profile were collected in under 5 min. In addition to shorter time periods, MREIT should also be able to monitor changes in conductivity over periods much larger than

that used in this study. Such extended durations would be useful when monitoring tumour growth and assessing response to treatment. For example, MREIT could be used to evaluate a patient's response to chemotherapy by measuring the (changing) conductivity of a suspicious lesion over several weeks.

Application of MREIT to human studies has seemed unpractical due to the large amounts of injected currents utilized in previous studies. Lower current levels result in a decrease in the signal-to-noise ratio (SNR) of the acquired magnetic flux density maps used in the reconstruction process. Oh *et al* (2005) recently acquired conductivity images of a biological tissue phantom in a 3T MRI system using the harmonic B_z algorithm. Their results show significant degradation in the reconstruction at as high as 12 mA of injected current. This is largely due to the use of the derivative operator on the magnetic flux density measurements, which amplifies errors from noise. Other reported biological tissue phantom studies utilizing gradient-based reconstruction methods used currents in excess of 24 mA. The results of this study demonstrate that MREIT is possible for injected currents as low as 900 μA. The SMM appears significantly more robust when reconstructing lower SNR data. Future work will search for the minimum levels of current needed for reconstructing accurate conductivity images.

Due to the geometry of the diffusion phantom, currents were restricted to flow within a slab of 1 cm thickness. In more intricate objects such as the human body, currents may flow throughout the entire object. Such 3D current flow will result in a decrease in the measurable magnetic flux density. The corresponding reduction in the SNR presents an additional challenge. To improve the SNR without increasing the injected current level, future work will optimize hardware and pulse sequence parameters. Use of a reconstruction algorithm capable of processing lower SNR data, such as the SMM, is also critical. The SMM has already been applied by Muftuler *et al* (2004) in reconstructing the conductivity distribution of an *in vivo* rat using 1 mA of injected current.

The maximum level of current that can safely be applied to humans depends on the frequency. In general, the safe current limit increases as the frequency increases. A majority of previously reported MREIT studies have utilized single cycle, long current pulses, essentially classifying them as dc with regards to safety standards. This study utilized alternating current in the form of multiple cycles of shorter alternating polarity pulses, with a cycle period of 10 ms (primary frequency component of 100 Hz). While safety levels at 100 Hz are only slightly higher than dc, the concept of using ac over dc has the advantage that future studies using higher frequencies will allow for safe application of larger current levels. Use of higher frequencies will also enhance the capacitive contributions to overall impedance, thus providing an additional source of information that may be of diagnostic relevance. Future work will test this pulse sequence and develop new pulse sequences for use in higher frequency MREIT.

5. Conclusions

By utilizing NaCl diffusion in an agarose gel phantom, we were able to demonstrate the ability of MREIT to monitor changes in an object's conductivity distribution over time. An injected current level of 900 μA was found acceptable for reconstructing accurate images when utilizing the iterative sensitivity matrix method with Tikhonov regularization. This is approaching the safe current levels for application in humans. The results of this study indicate that human MREIT should be feasible in the near future, and that this modality can be used not only for acquiring static images, but also used for performing dynamic studies.

Acknowledgments

This study was supported in part by grants NIH/NCI R01 CA114210, DOD DAMD17-02-1-0326, and DOD W81XWH-04-1-0446a.

References

Baumann S B, Wozny D R, Kelly S K and Meno F M 1997 The electrical conductivity of human cerebrospinal fluid at body temperature *IEEE Trans. Biomed. Eng.* **44** 220–3

Birgul O, Eyuboglu B M and Ider Y Z 2003a Current constrained voltage scaled reconstruction (CCVSR) algorithm for MR-EIT and its performance with different probing current patterns *Phys. Med. Biol.* **48** 653–71

Birgul O, Eyuboglu B M and Ider Y Z 2003b Experimental results for 2D magnetic resonance electrical impedance tomography (MR-EIT) using magnetic flux density in one direction *Phys. Med. Biol.* **48** 3485–504

Crank J 1975 *The Mathematics of Diffusion* (New York: Oxford University Press)

Fuoss R M and Onsanger L 1957 Conductance of unassociated electrolytes *J. Phys. Chem.* **61** 668–82

Golub G H, Hanse P C and O'Leary D P 1999 Tikhonov regularization and total least squares *SIAM J. Matrix Anal. Appl.* **21** 185–94

Ider Y Z and Birgul O 1998 Use of the magnetic field generated by the internal distribution of injected currents for electrical impedance tomography (MR-EIT) *Elektrik* **6** 215–25

Ider Y Z and Muftuler L T 1997 Measurement of AC magnetic field distribution using magnetic resonance imaging *IEEE Trans. Med. Imaging* **16** 617–22

Ider Y Z and Onart S 2004 Algebraic reconstruction for 3D magnetic resonance-electrical impedance tomography (MREIT) using one component of magnetic flux density *Physiol. Meas.* **25** 281–94

Jossinet J 1998 The impedivity of freshly excised human breast tissue *Physiol. Meas.* **19** 61–75

Khang H S, Lee B I, Oh S H, Woo E J, Lee S Y, Cho M Y, Kwon O, Yoon J R and Seo J K 2002 J-substitution algorithm in magnetic resonance electrical impedance tomography (MREIT): phantom experiments for static resistivity images *IEEE Trans. Med. Imaging* **21** 695–702

Kwon O, Woo E J, Yoon J R and Seo J K 2002 Magnetic resonance electrical impedance tomography (MREIT): simulation study of J-substitution algorithm *IEEE Trans. Biomed. Eng.* **49** 160–7

Lee B I, Oh S H, Woo E J, Lee S Y, Cho M H, Kwon O, Seo J K and Baek W S 2003 Static resistivity image of a cubic saline phantom in magnetic resonance electrical impedance tomography (MREIT) *Physiol. Meas.* **24** 579–89

Mikac U, Demsar F, Beravs K and Sersa I 2001 Magnetic resonance imaging of alternating electric currents *Magn. Reson. Imaging* **19** 845–56

Muftuler L T, Hamamura M, Birgul O and Nalcioglu O 2004 Resolution and contrast in magnetic resonance electrical impedance tomography (MREIT) and its application to cancer imaging *Technol. Cancer Res. Treat.* **3** 599–609

Oh S H, Lee B I, Woo E J, Lee S Y, Kim T S, Kwon O and Seo J K 2005 Electrical conductivity images of biological tissue phantoms in MREIT *Physiol. Meas.* **26** S279–88

Park C, Kwon O, Woo E J and Seo J K 2004a Electrical conductivity imaging using gradient B_z decomposition algorithm in magnetic resonance electrical impedance tomography (MREIT) *IEEE Trans. Med. Imaging* **23** 388–94

Park C, Park E J, Woo E J, Kwon O and Seo J K 2004b Static conductivity imaging using variational gradient B_z algorithm in magnetic resonance electrical impedance tomography *Physiol. Meas.* **25** 257–69

Reddy J N 1993 *An Introduction to the Finite Element Method* (New York: McGraw-Hill)

Schantz E J and Lauffer M A 1962 Diffusion measurements in agar gel *Biochem.* **1** 658–63

Scott G C, Joy M L G, Armstrong R L and Henkelman R M 1991 Measurement of nonuniform current density by magnetic resonance *IEEE Trans. Med. Imaging* **10** 362–74

Seagar A D, Barber D C and Brown B H 1987 Theoretical limits to sensitivity and resolution in impedance imaging *Clin. Phys. Physiol. Meas.* **8** A13–31

Seo J K, Yoon J R, Woo E J and Kwon O 2003 Reconstruction of conductivity and current density images using only one component of magnetic field measurements *IEEE Trans. Biomed. Eng.* **50** 1121–4

Surowiec A J, Stuchly S S, Barr J R and Swarup A 1988 Dielectric properties of breast carcinoma and the surrounding tissues *IEEE. Trans. Biomed. Eng.* **35** 257–63

Contrast and spatial resolution in MREIT using low amplitude current

Ozlem Birgul , Mark J Hamamura, L Tugan Muftuler, and Orhan Nalcioglu

Tu and Yuen Center for Functional Onco Imaging, University of California at Irvine
e-mail: *obirgul@uci.edu*

Abstract. Magnetic resonance - electrical impedance tomography employs low amplitude currents injected or induced inside an object. The additional magnetic field due to these currents results in a phase in the MR images. A modified fast spin-echo sequence was used to measure this magnetic field, which simply is a scaled phase of the MR image. Finite element method was used for the solution of the forward problem. An iterated sensitivity matrix based algorithm was developed for the inverse problem. Resulting ill-conditioned matrix equation was regularized using Tikhonov method and solved using a conjugate gradient solver. The spatial and contrast resolution of the technique was tested using agarose gel phantoms.

PACS numbers: 87.63.Pn, 87.61.-c

Submitted to: *Phys. Med. Biol.*

1. Introduction

MREIT (magnetic resonance-electrical impedance tomography) is a recently developing imaging modality that reconstructs conductivity images from the magnetic flux density generated due to a current distribution in a volume conductor. The main advantages of the MREIT are the non-invasive measurement of the field from inside the object (that increases the sensitivity to inner regions), higher number of measurements without being limited to detection probes (that improves the resolution), and availability of the MR image for accurate modeling of the geometry and boundary conditions.

Although it is possible to detect locations of lesions in breast cancer using techniques such as x-ray mammography due to problems of specificity, many women undergo unnecessary biopsies. Therefore, new highly specific techniques are needed to decrease the false positive results while maintaining the high sensitivity (Elmore *et al* 2002). Since the conductivity values of malignant, benign, and normal tissues are significantly different, this information can be used in tumor classification (Surowiec *et al* 1988) to improve specificity.

MREIT reconstruction algorithms can be grouped into two depending on the type of data they use. Earlier algorithms generated current density maps from the measurements as an intermediate step towards conductivity reconstruction. J-substitution method, (Khang *et al* 2002), current constrained-voltage scaled reconstruction (CCVSR) (Birgul *et al* 2003a), and equipotential projection based reconstruction (Ozdemir *et al* 2004) are examples of this type of algorithms. The disadvantage of these algorithms is the need for two or three components of the magnetic flux density, which requires rotation of the object inside the magnet. Other algorithms use magnetic flux density measurements directly and measurement of only one component is sufficient. Sensitivity based reconstruction (Ider and Birgul 1998, Birgul *et al* 2003b, Muftuler *et al* 2004), algebraic reconstruction technique (Ider and Onart 2004), variational gradient B_z algorithm (Park *et al* 2004a), and gradient B_z decomposition algorithm (Park *et al* 2004b) fall into second group of algorithms.

Several studies have been carried out experimentally using phantoms to evaluate the performance of MREIT (Birgul *et al* 2003b, Lee *et al* 2003, Oh *et al* 2004). The major limitation in practice is the amplitude of the current required to achieve an acceptable signal-to-noise ratio. Lee *et al* (2003) reported relative L^2-errors of 25.5% and 32.3% with denoising and without denoising with an injected current of 28 mA. Birgul and Ider (2003a) carried out experiments with 25 mA peak current and reconstructed conductivity images with 13-17% error without using any denoising techniques. Oh *et al* (2004) reported 11-35% error when the current was 24 mA. Muftuler *et al* presented results for phantoms and an *in-vivo* tumor bearing animal with current levels that are as low as 2-4 mA. In their study, the ratio of the conductivity of a region of interest to a reference was investigated, therefore, no voltage measurements were acquired resulting in relative conductivity images.

In this study, we used an iterative version of the reconstruction algorithm outlined

by Muftuler *et al* (2004) with Tikhonov regularization. This reduces noise sensitivity of reconstruction and enables one to use lower current levels, which is critical for human applications. The pulse sequence used in data acquisition was also improved so that the noise in the magnetic flux density measurements for low current levels were acceptable. Several agarose phantoms were prepared to characterize the contrast and spatial resolution performance. The details of data acquisition, image reconstruction, and reconstructed images are presented in the following sections.

2. Methods

Reconstruction of conductivity involves two basic steps. The first step is the measurement of magnetic flux density using magnetic resonance imaging. This step involves MRI data acquisition using a modified spin echo pulse sequence and generation of magnetic flux density images from the MRI phase images using scaling. In the second step, these images are used as input data in the inverse problem of finding conductivity from the magnetic flux density information. In this section the components of the hardware and pulse sequence used for data acquisition are presented first. Then, the reconstruction algorithm based on sensitivity matrix is explained.

2.1. Experimental Setup

The acquisition system for the MREIT consists of a conventional whole body MRI system and a current source that is synchronized with the RF pulses generated by the MRI system.

The MRI system has a 4T whole body Magnex magnet with a whole body gradient coil set that provides up to 3G/cm gradient fields. A 13 channel room-temperature high-order shim coil set was used to minimize field inhomogeneities. This system was interfaced with a MRRS console (Magnetic Resonance Research Systems, Guildford, UK) that has broadband RF transmit and receive channels. A 16 leg, quadrature, high-pass birdcage coil with 10 cm diameter and 18 cm length was designed and built in-house for the MREIT experiments.

The current source uses pulses generated by the MRI console and a voltage-to-current converter that uses three LM741 OPAMPs. This current source was triggered by a TTL pulse generated by the scanner computer. The current cables were connected to the object through several RF chokes and low pass filters to suppress RF coupling. These cables were fixed on an acrylic structure that also supports the phantom. The orientation of the cables is critical so that only the effect of current flowing through the object creates a phase in the MR image. The rigid support guarantees that external currents flow parallel to the main magnetic field (z-direction) so that their effect is zero.

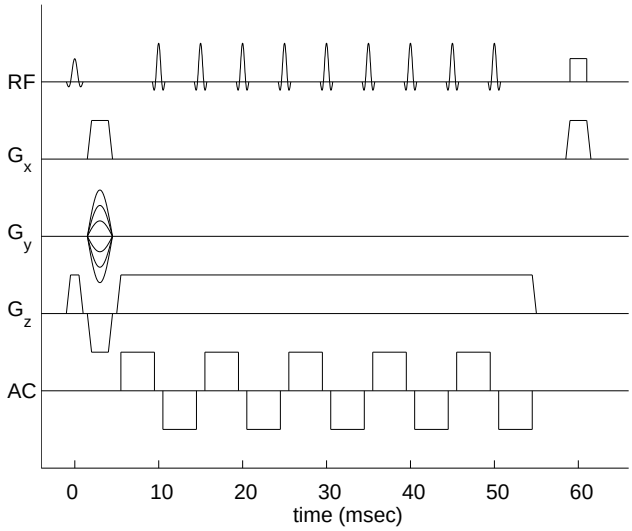

Figure 1. Sample pulse sequence used in the MREIT experiments (parameters used are given in the results section).

2.2. Pulse Sequence

The MREIT data was collected using the pulse sequence shown in Fig. 1. In this pulse sequence, RF pulses are synchronized with the current pulse train so that phases generated in positive and negative cycles cancel each other out. By synchronizing successive π pulses to half cycles of the current, the phase shift accumulates; however, it is superimposed onto the phase component due to main and gradient field inhomogeneities. To extract the current-only component, the experiment is repeated twice with opposite current polarities. When the difference is taken, system-dependent phase shifts cancel out and current-dependent phase,Φ_I, is obtained as

$$\Phi_I(r) = 2\gamma N T_{pulse} B_z(r) \tag{1}$$

where γ is the gyromagnetic ratio, N the number of cycles of injected current, $B_z(r)$ the amplitude of z-component of the current-generated magnetic field at point r, and T_{pulse} is the duration of each current pulse. Measurement of this phase shift allows for calculation of the (z-component) of magnetic field distribution. More information about extraction of magnetic flux density from MR images can be found in Muftuler *et al* (2004).

2.3. Image Reconstruction

A sensitivity-based reconstruction algorithm that uses one component (z-component) of the magnetic flux density is used. The forward relation between conductivity and magnetic flux density and linearization of the forward transformation are explained in detail in Birgul *et al* (2003b). Finite element method (FEM) with first order triangular elements are used for the discretization of the forward problem defined by Laplace's equation and Neumann boundary conditions (Silvester and Ferrari 1996).

Compared to sensitivity based reconstruction algorithms reported before (Birgul *et al* 2003b, Muftuler *et al* 2004), the major differences of the algorithm used in this study are:

(i) using conjugate gradient solver (CGS) instead of truncated SVD. This eliminated the requirement of large decomposition matrices, which enables faster reconstruction.

(ii) introducing Tikhonov regularization instead of truncation. The criteria used in selection of the optimum regularization parameter is explained later in this section. This eliminates operator dependence.

(iii) iterating the algorithm to improve accuracy even for large conductivity perturbations.

In the reconstruction process, a uniform conductivity is assumed as the initial distribution and sensitivity matrix is calculated analytically (Birgul *et al* 2003b). Resulting matrix equation that approximates the relation between conductivity and magnetic flux density perturbations is given by:

$$\Delta \mathbf{b} = \mathbf{S} \Delta \sigma \tag{2}$$

where $\Delta \mathbf{b}$ is the difference between measured magnetic flux density and the magnetic flux density corresponding to initial distribution, $\Delta \sigma$ is the change with respect to initial conductivity distribution and $\mathbf{S}$ is the sensitivity matrix that gives the relation between changes in magnetic flux density and conductivity. Due to noise in the data, some form of regularization is required to be able to solve the system in Eq. 2. Including Tikhonov regularization parameter, λ, the matrix equation becomes,

$$(\mathbf{S}^T \mathbf{S} + \lambda \mathbf{I}) \Delta \sigma = \mathbf{S}^T \Delta \mathbf{b} \tag{3}$$

where $\mathbf{I}$ is the identity matrix. The matrix equation is solved for different values of λ using conjugate gradient method and the optimum regularization value is selected as the one minimizing the difference,

$$\min_{\lambda} \sum_{i=1}^{m} \| B_{meas,i} - B_{calc,i}(\lambda) \| \tag{4}$$

where m is the total number of measurement points, B_{meas} is the measured magnetic flux density, and B_{calc} is the flux density calculated using reconstructed conductivity. For iterations, calculated conductivity distribution is assigned as the initial value and the steps starting with sensitivity matrix calculation are repeated until the change in conductivity two consecutive iterations are below a defined threshold. The flowchart of the algorithm is given in Fig. 2.

3. Results

3.1. Phantom Preparation

Various agarose gel phantoms were used for the experiments. The agarose powder (OmniPur brand) was mixed with different concentrations of *NaCl* to generate different

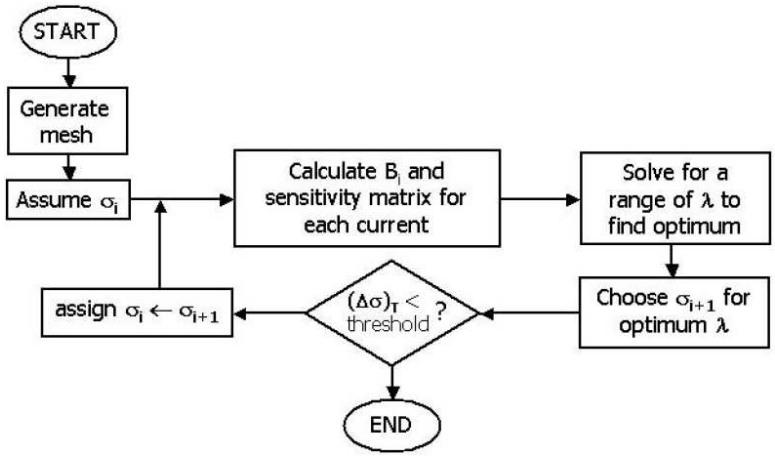

Figure 2. Flowchart of the sensitivity based iterative reconstruction algorithm.

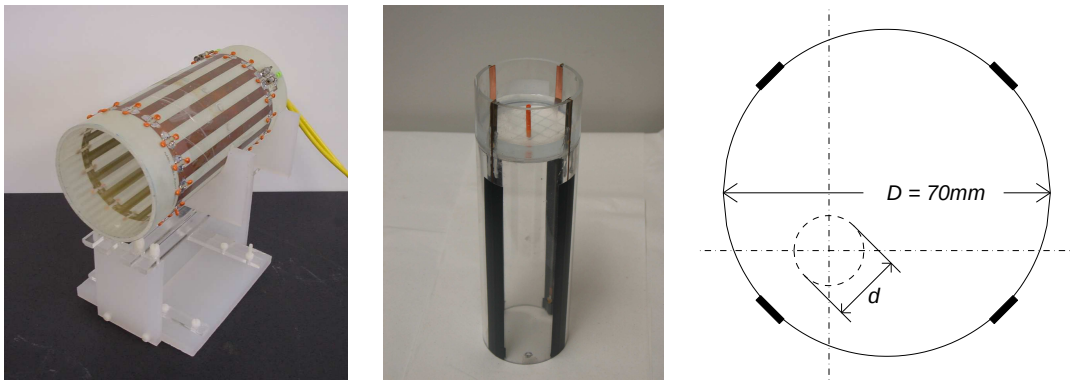

Figure 3. (a) Home-built RF coil (b) Phantom (c) Phantom description

conductivity values. 2 gr of agarose powder was used per 100 mL of water. Gels were poured into an acrylic cylinder with an inner diameter of 7 cm and height of 1 cm (Fig. 3). Four electrodes made from 6 mm-wide copper tape with conducting glue were placed at $\{\frac{\pi}{4}, \frac{3\pi}{4}, \frac{5\pi}{4}, \frac{7\pi}{4}\}$ along the inner wall, that could provide up to 6 different current injection pairs. It has been shown that at least two independent current injection profiles are required for the uniqueness of the solution (Ider *et al* 2003) and we selected two current injection setups that used opposite electrode pairs. Current carrying wires were placed precisely in the z-direction to eliminate any contribution from the currents flowing in those wires. Wires were mounted on acrylic support beams to establish rigidity.

For all cases, 1 gr NaCl/100 gr water was used as the the background solution. Different amounts of *NaCl* was used to create different object values. Although *NaCl* amounts were chosen as multiples of the background reference, due to nonlinearity the conductivity values were not linearly scaled. For the accurate evaluation of the reconstruction values, we measured the conductivity of all solutions independently using a 4-electrode conductivity measurement cell. The measured values are given in Table 1.

Table 1. Measured conductivity values for different *NaCl* concentrations

NaCl (grs/100mL)	0.25	1.00	1.20	2.00	4.00	7.00	10.00
Conductivity (S/m)	0.43	1.61	1.88	3.02	5.68	9.08	11.22

3.2. Pulse Sequence and Current Parameters

The pulse sequence in Fig. 1 was used with the following parameters:

repetation time	T_R	500 msec
echo time	T_E	58 msec
field of view	FOV	100 mm
number of averages	NEX	4
slice thickness	Δw	5 mm
image matrix		64×64
number of current cycles	N	5
current peak	I_p	1 mA
current frequency	f	100 Hz
number of profiles		2

Note that although NEX is listed as four, since the pulse sequence was applied twice with opposite polarities, the effective number of averages was equivalent to 8. The current was applied at 100 Hz with 1 mA peak. The current pulse can be expanded as a summation of infinite sine waves with frequencies corresponding to odd harmonics of the main frequency. Due to timing of the π pulses, only the component at the main harmonic frequency will accumulate additional phase and this scale must be included in the calculations. For each current profile, data acquisition took about 4 mins with the above parameters resulting in 8 min total acquisition time. For phantom studies, we did not acquire high resolution anatomical images prior to the MREIT experiment and magnitude images of the MREIT experiment were used for mesh generation. For cases with irregular boundaries, such as small animal imaging, an accompanying high resolution anatomical image would increase the accuracy of the forward solution.

3.3. Reconstruction Parameters

A finite element mesh with 1089 nodes and 2048 triangular elements was generated for the forward solver. 6 mm electrodes covers 2 elements with 3 nodes at the boundary. Phase measurements were acquired on a rectangular grid of 64×64 for the whole field of view and approximately $1000 - 1100$ of these fell into the object region in the mask. Note that the number of measurements, m, depend on the mask specific to each case defined by the signal to noise ratio. The sensitivity matrices for each current profile were stacked to have the combined sensitivity matrix, which is indicated by $\mathbf{S}$ in Eq. 3, of size $2m \times 2048$. For the first iteration the maximum singular value, σ_{max}, and condition number, $\sigma_{max}/\sigma_{min}$, of $\mathbf{S}^T\mathbf{S}$ are $1.13 * 10^{-12}$ and $5.2 * 10^{19}$ respectively when the units of

distance, conductivity, and current amplitude are cm, S/cm, and mA respectively with an initial conductivity distribution of $0.016 S/cm$. Tikhonov regularization parameter, λ, is in the order of 10^{-14} for the first iteration which is in the order of 1/100 of the maximum singular value. The iterations are stopped when the change in overall conductivity is below 3% of the previous iteration and this corresponds to 4-6 iterations.

3.4. Spatial Resolution

In order to understand the spatial resolution for low amplitude currents, phantoms that contain objects with different diameters (3 mm, 5 mm, and 8 mm) and extreme conductivity cases (insulator (-ins) and high conductivity (-cond)) were reconstructed. For the insulator cases, hollow cylinders filled with the same agarose- $NaCl$ solution as the background were used. For the high conductivity cases, a solution with 10 gr$NaCl$/100 gr water, which gives a 6.70:1 contrast with respect to background, was used.

In Fig. 4(a)-(b) image reconstructed for 5mm-cond case is given for two different views. The full-width at half-maximum (FWHM) values were calculated in two orthogonal profiles passing through the center of the object (FWHMx for x direction and FWHMy for y direction). In Fig. 4(c)-(d), the profiles and the baseline and half-maximum levels for the measurement are shown. Similarly, FWHMx and FWHMy were calculated for the 5mm-ins case using Fig. 4(e)-(f). The same analysis was repeated for 3mm-cond, 3mm-ins, 8mm-cond, and 8mm-ins cases. The images reconstructed for conductivity and insulator cases are given in Figs. 5 and 6, respectively. FWHM values for all cases are summarized in Table 2.

From these values, it is seen that for all cases, the spread is more for the conductor case than the insulator case. Ideally, the spread functions are to be obtained using extreme conductivity cases using a perfect conductor (∞ conductivity) and a perfect insulator (zero conductivity). Experimental insulator case matches this condition closest but the conductor case phantom uses finite conductivity values. Since the $NaCl$ concentrations in the object and background are different due to diffusion, the conductivity of the object decreases and the FWHM increases with time (Hamamura *et al* (2005a), Hamamura (2005b)). Hamamura (2005b) carried out extensive analysis on diffusion effects in agarose phantoms over a 12 hour period by reconstructing images at 11 different time points. After 1 hour, the FWHM value of a 12 mm-diameter object increases from 11.98 mm to 12.44 mm. This may explain the difference between the spread functions for -ins and -cond cases. For example the 8mm-ins case, the FWHM value is equal to the object size whereas for the 5mm-ins case, it is 20% more than the object size.

Another difference between the conductor and insulator cases is the background noise in the reconstructed images. For all cases, conductor images are less noisy compared to the insulator cases of the same size object case. The main reason for this difference is the loss in the measured signal amplitude in perfect insulator regions.

Table 2. Spatial Resolution Analysis

case	FWHMx (mm)	FWHMy (mm)	peak object (S/m)	mean background (S/m)
3mm-ins	4.2	5.3	0.78	1.58
3mm-cond	8.3	7.0	3.01	1.50
5mm-ins	6.0	6.0	0.44	1.61
5mm-cond	8.7	7.4	5.68	1.42
8mm-ins	7.9	8.2	0.27	1.59
8mm-cond	10.6	9.5	6.00	1.37

The highest change in magnetic flux density occurs at the object boundary, however, due to the insulator shell, this cannot be accurately measured using MRI. Especially for the 3mm case where the total volume of the insulator shell becomes significant compared to the object volume, the signal level drops significantly resulting in low SNR. Therefore, this is limit imposed by the phantom preparation rather than the MREIT technique itself.

We also looked at the peak reconstructed values (maximum/minimum conductivity for conductor/insulator cases) in the object and mean conductivity in the background and these values are also listed in Table 2. Note that the significant measure for spatial resolution analysis is the FWHM value, however, the numerical conductivity values are also listed to provide readers an idea. For all cases, expected background conductivity is 1.61 S/cm. For the insulator cases, the expected object conductivity is zero. For the high conductor case, although the true conductivity value is 11.22 S/m, reconstructed values are much lower, which could be expected due to diffusion and small object size (PSF effect). If the peak values for different cases are compared, it is seen that as the object size increases, the value increases, towards the true conductivity value.

3.5. Contrast Resolution

In order to understand the system performance at different contrast levels, 15mm-diameter objects with five different conductivity values between the two extreme cases used in the spatial resolution analysis were selected. The true conductivity and ratio values and reconstructed peak object and mean background values are summarized in Table 3. In the first case, the object conductivity is set lower than the background conductivity (0.36:1 contrast case, Case I). In the top row of Fig. 7, reconstructed image and one of the profiles is plotted. Due to high errors at the boundary, the object is not clearly visible in the image, however, it is well resolved in the profile image. Next, we used a low contrast conductor object where the object conductivity was 17% more than the background (Case II). For this case, the noise effects are dominant in the image (Fig. 7, second row) and the object can hardly be seen in the profile images. Then we increased the conductivity further using three contrast levels, 1.88:1, 3.53, and 5:64 (Cases III, IV, and V, respectively)and results are presented in Fig. 7 and Table 3. The

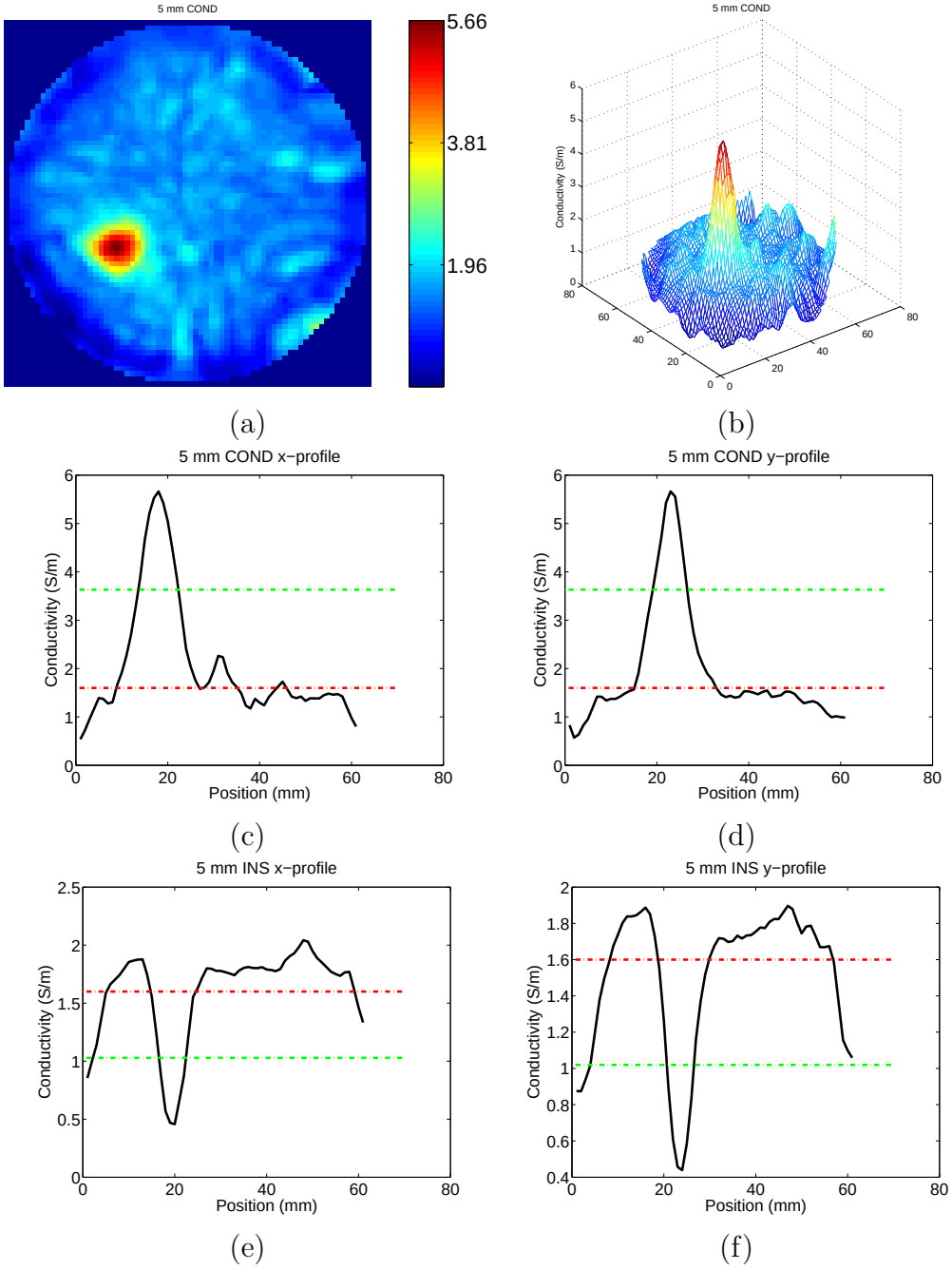

Figure 4. Spatial resolution analysis using 5mm object (a) Image plot for 5mm-cond (b) Mesh plot for reconstructed conductivity for 5mm-cond (c) Profile through object center along x-direction for 5mm-cond (d) Profile along y-direction for 5mm-cond (e) Profile along x-direction for 5mm-ins (f) Profile along y-direction for 5mm-ins

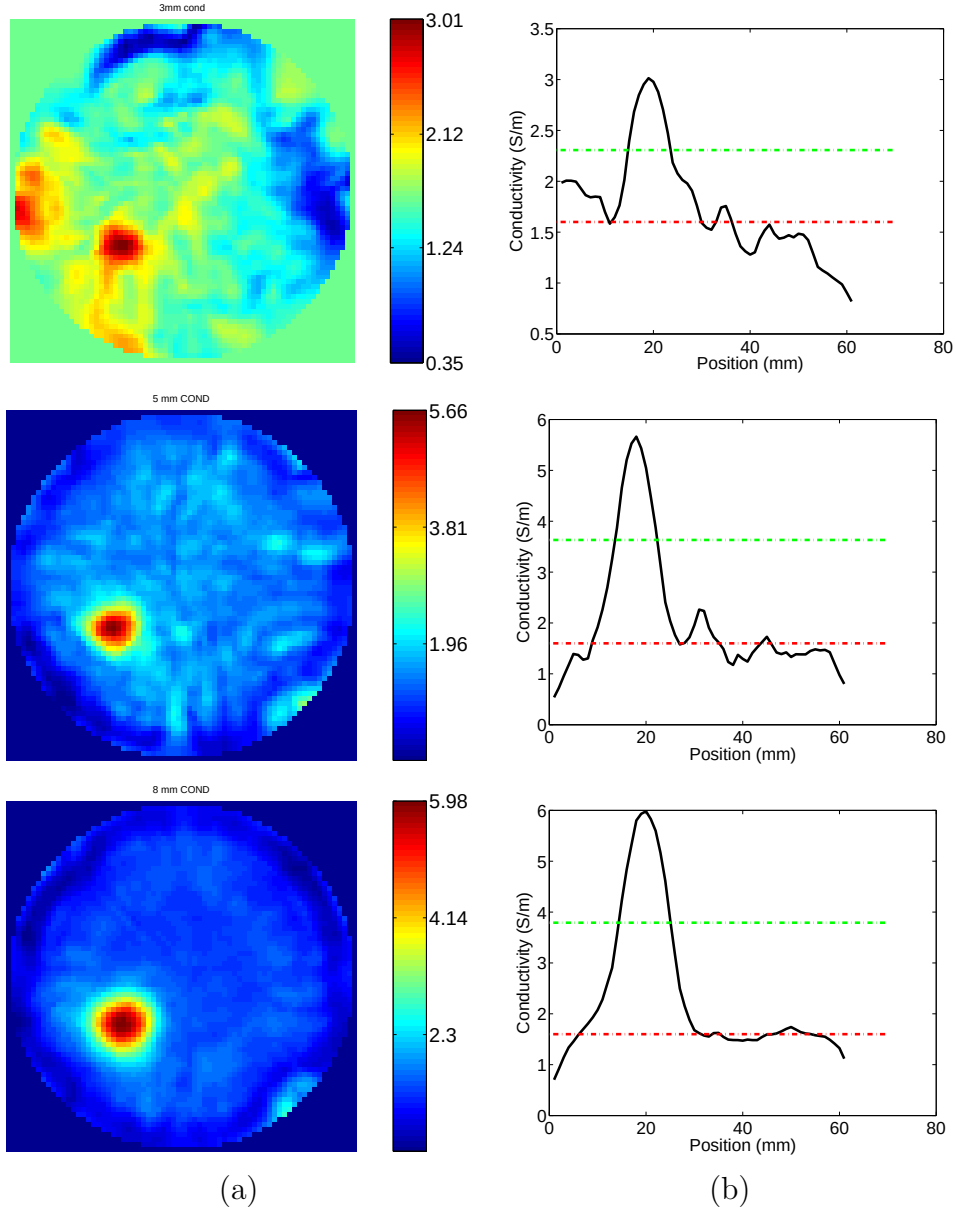

Figure 5. Reconstructed conductivity images for 3, 5, and 8mm conductor objects and corresponding profiles

noise in the background is becomes less significant as the object contrast increases.

For the conductor cases III, IV, and V, the peak reconstructed values are lower than the true values which is expected due to the diffusion effect explained in the previous section. The same effect results in a higher conductivity peak in the object when the object has lower conductivity (Case I) and the direction of diffusion is reversed.

In Fig. 8, the graph for true contrast ratio versus reconstructed conductivity ratio is presented. In this plot, the dashed line corresponds to ideal reconstruction. It is seen that the deviation from the theoretical case is more for higher conductivity values, which could be due to nonlinear nature of the governing differential equation.

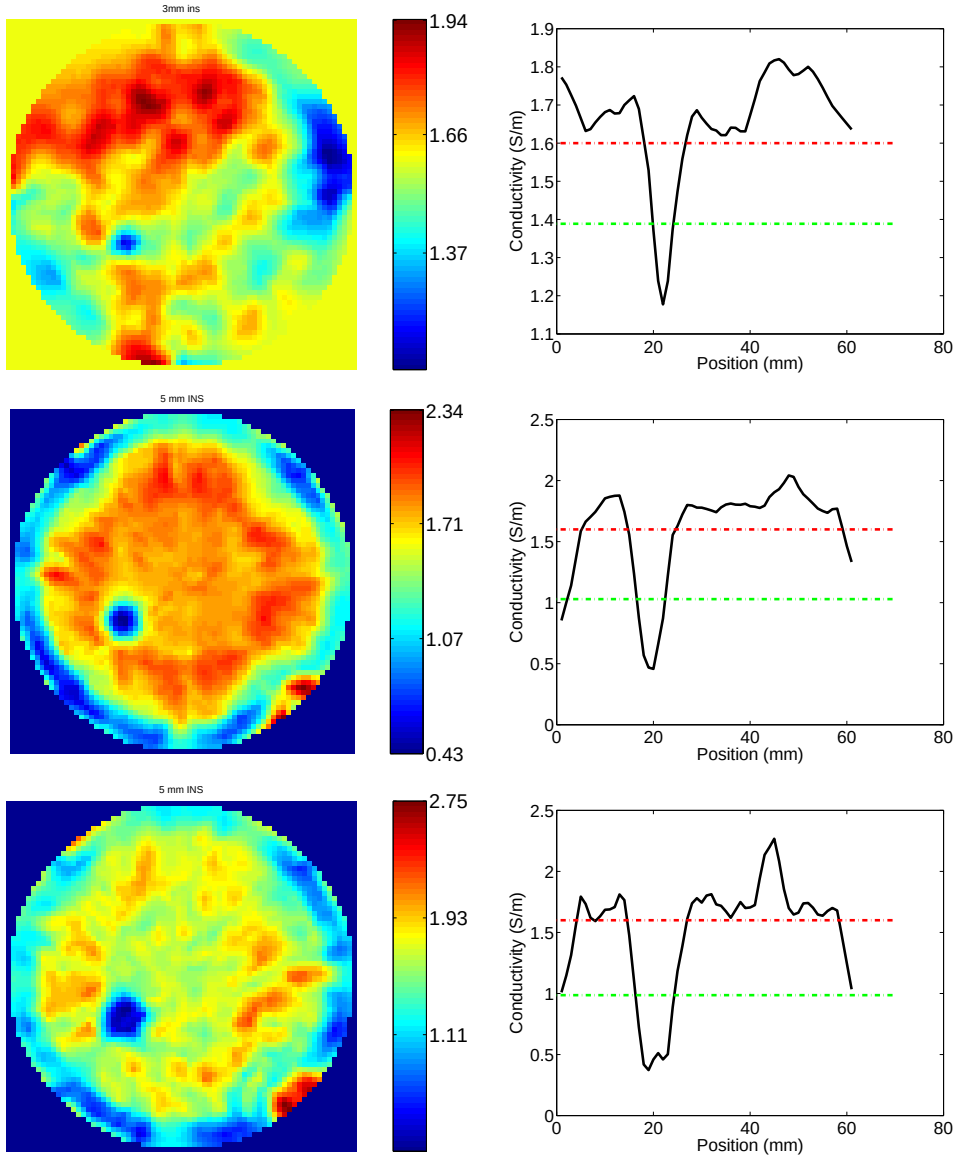

Figure 6. Reconstructed conductivity images for 3, 5, and 8mm insulator objects and corresponding profiles

Table 3. Contrast Resolution Analysis

NaCl (gr)	True Ratio	Recon Ratio	True Peak	Recon Peak	True Backg.	Recon Backg
0.25	0.36	0.44	0.43	0.70	1.61	1.60
1.2	1.17	1.32	1.88	2.09	1.61	1.58
2	1.88	1.70	3.02	2.61	1.61	1.54
4	3.53	3.45	5.68	4.71	1.61	1.36
7	5.64	5.03	9.08	6.00	1.61	1.19

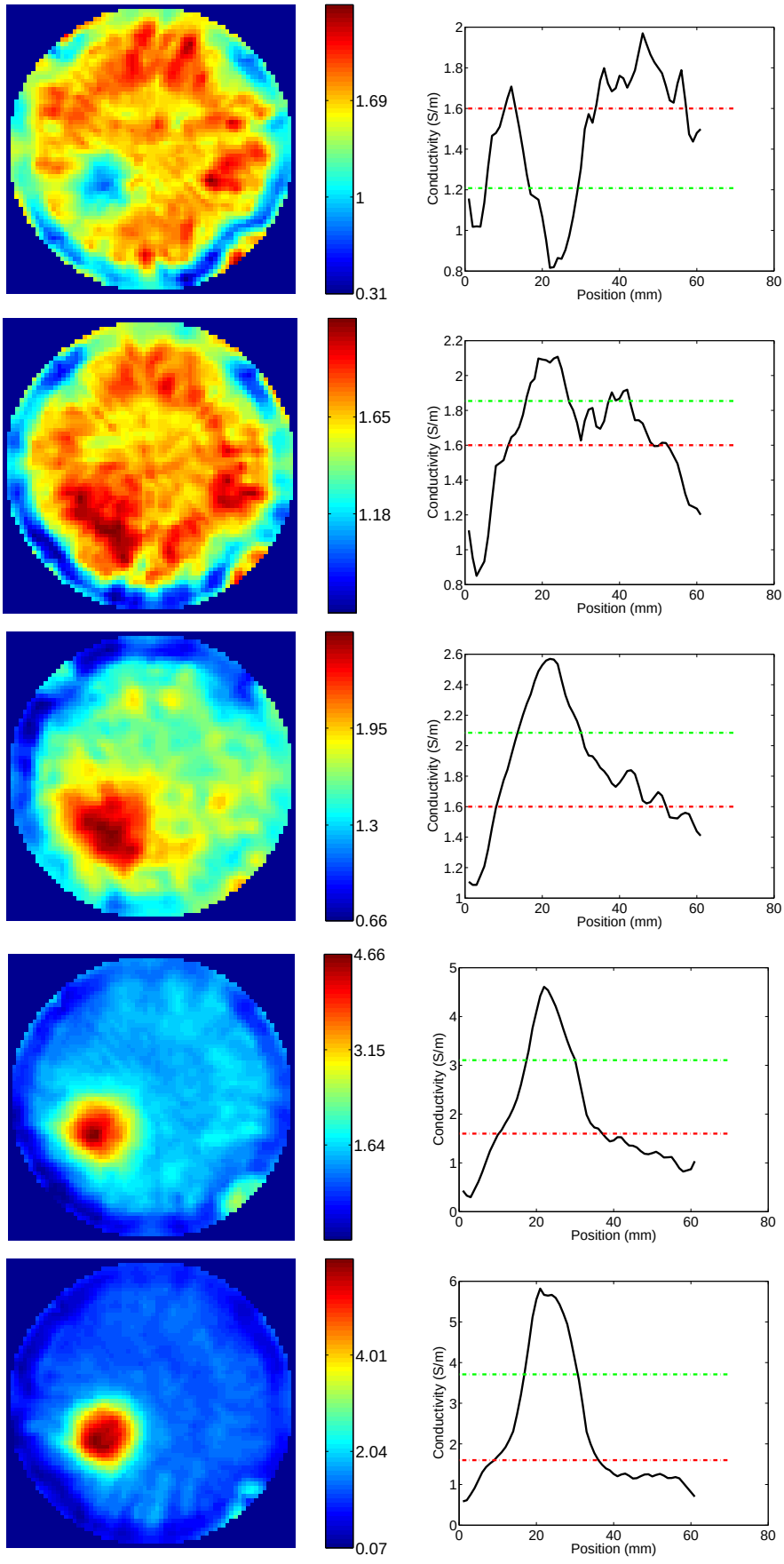

Figure 7. Reconstructed images and corresponding profiles for different contrast objects. From top to bottom (I) 0.36:1, (II) 1.17:1, (III) 1.88:1, (IV) 3.53:1, (V) 5.64:1 contrast cases. Values are listed in Table 3.

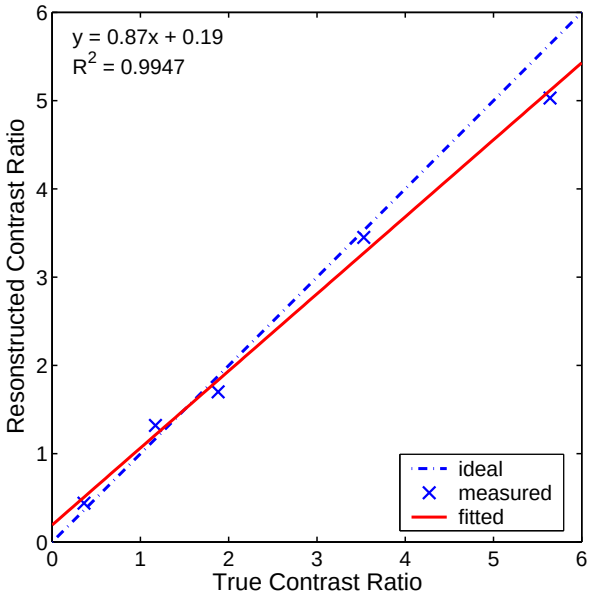

Figure 8. Comparison of experimental contrast ratios obtained to the ideal case

4. Discussion

In this study, contrast and spatial resolution limits in MREIT are investigated using low level AC currents. Majority of the previous studies on MREIT reported results using higher current levels ($> 24mA$) which may not be suitable for human applications. We used 1 mA peak current in our experiments and generated conductivity images with better resolution and accuracy compared to other conductivity imaging techniques. Current levels comparable to the ones in our study are used in Muftuler's (Muftuler *et al* 2004) preliminary study where a couple of phantom results and a small animal result were presented. Since the pulse sequence and reconstruction algorithm are improved, noise performance is also improved.

Small objects with extreme conductivity values were prepared for understanding the spatial resolution limits. 3 mm, 5 mm and 8 mm insulator and high conductor objects were used. Our results suggests that the spatial resolution is 3 mm or better. Due to diffusion effects, for high conductivity cases, the object starts spreading in the conductivity map and an accurate spread measurement is not possible. In order to understand the exact resolution limit, we tried using smaller insulator objects, however since we cannot get enough MRI signal from inside such a small insulator object, it was not possible to take measurements from such phantoms. The FWHM of 3mm-ins object was measured to be 4.2 mm. Therefore, we can state that the resolution is around 3 mm or better in a $7cm$ object when 1 mA current is used.

Several phantoms with different conductivity values were prepared to understand the contrast resolution limits of the low current MREIT. Conductivity values ranging from approximately one-fourth of the background to six times the background were used. For the low conductivity case, although the object was clearly resolved, the background

error, especially at the boundary was very high. For the low contrast conductor object, where conductivity of the object was 17% higher than the background a similar result is obtained and object was not resolved. It has been reported by several groups that highest error in measurements is observed at the boundary. In a recent study Hamamura (2005) suggested several masking and correction algorithms to eliminate these problems. For higher conductivity contrast cases, the boundary effects are not as significant. Diffusion of *NaCl* from higher to lower concentration also effects the reconstruction here. For low conductivity case, diffusion is from background towards object and reconstructed object conductivity is higher. For higher conductivity cases, the direction of diffusion is reversed and reconstructed value are lower than the expected values as can be seen from Fig. 8.

In this study, in order to reduce total data acquisition time, we only used two current injection profiles, which is the minimum required for uniqueness and was sufficient. The total data acquisition time was 8 min for this case. Depending on the application, more current injection profiles may be required. If the data acquisition time is limited, trade off between current profiles and number of the averages must be investigated for optimum SNR.

The first step in the image reconstruction is the selection of the initial conductivity distribution. Theoretically as long as a uniform conductivity distribution is chosen, the magnetic flux density is independent of its value. When we did reconstruction using real data, however, we observed that initial conductivity distribution effects the convergence speed. For the cases presented here, the results converged in 4-6 iterations if the initial conductivity distribution was equal or lower than the background and higher number of iterations was required if the initial conductivity distribution was higher (approximate ten fold) than the background. Also note that reconstruction results provide relative conductivity values, which is a scaled version of the true values, due to the fact that only the magnetic flux density measurements are used. For breast cancer, the relative conductivity value of tumor with respect to background or a reference organ would provide the necessary information. However, if the absolute conductivity values are required, the scaling factor can be determined using a single voltage measurement.

5. Conclusions

Results presented here are critical in understanding the limits of MREIT at lower currents which is required for translation of the study to animal and ultimately to human applications. Comparison of our results with the literature suggests that using multiple current pulses provides better signal-to-noise in measurements and sensitivity based reconstruction is less susceptible to noise in measurements compared to the gradient based algorithms.

Acknowledgments

This work was supported in parts by The U.S. Army Medical Research and Materiel Command under W81XWH-04-1-0446 grant and NIH /NCI Award R01-114210.

6. References

Birgul O, Eyuboglu B M, and Ider YZ, "Current constrained voltage scaled reconstruction (ccvsr) algorithm for MREIT and its performance with different probing current performance," *Physics in Medicine and Biology*, vol. 48, no. 21, pp. 653–671, 2003.

Birgul O, Eyuboglu B M, and Ider YZ, "Experimental results for 2d magnetic resonance electrical impedance tomography (MREIT) using magnetic flux density in one direction," *Physics in Medicine and Biology*, vol. 48, no. 21, pp. 3485–3504, 2003.

Elmore J G, Barton M B, Moceri V M, Polk S, Arena P J, and Fletcher S W, "Screening mammograms by community radiologists: variability in false-positive rates," *Journal of National Cancer Institute*, vol. 94, no. 18, pp.1376–1380, 2002.

Hamamura M J, Muftuler L T, Birgul O, and Nalcioglu O, "Tracking of sodium diffusion in agarose using MREIT," in *ISMRM*, 2005.

Hamamura M J, "Electrical impedance tomography using magnetic resonance imaging," , *University of California at Irvine, PhD Thesis*, 2005.

Ider Y Z and Birgul O, "Use of magnetic field generated by the internal distribution of injected currents for electrical impedance tomography (MREIT)," *Elektrik Turkish J. Electr. Eng. And Comput. Sci.*, vol. 6, pp. 215–225, 1998.

Ider Y Z, Onart S , and Lionheart W R B, "Uniqueness and reconstruction in magnetic resonance-electrical impedance tomography (MREIT)," *Physiological Measurement*, vol. 24, pp. 591–604, 2003.

Khang H S, Lee B I, Oh S H, Woo E J, Lee S Y, Cho M H, Kwon O, Yoon J R, and Seo J K, "J-substitution algorithm in magnetic resonance electrical impedance tomography (mreit): Phantom experiments for static resistivity images," *IEEE Transactions on Medical Imaging*, vol. 21, no. 6, pp. 695–702, 2002.

Kim Y J, Kwon O, Seo J K, and Woo E J "Uniqueness and convergence of conductivity image reconstruction in magnetic resonance electrical impedance tomography," *Inverse Problems*, vol. 19, pp. 1213–1225, 2003.

Lee B I, Oh S H, Woo E J, Lee S Y, Cho M H, Kwon O, Seo J K, and Baek W S "Static resistivity image of a cubic saline phantom in magnetic resonance electrical impedance tomography," *Physiological Measurement*, vol. 24, pp. 579–589, 2003.

Lee J Y "A reconstruction formula and uniquess of conductivity in mreit using two internal current distributions," *Inverse Problems*, vol. 20, pp. 847–858, 2004.

Muftuler L T, Hamamura M J, Birgul O, and Nalcioglu O, "Resolution and contrast in magnetic resonance electrical impedance tomography (mreit) and its application to cancer imaging," *Technology in Cancer Research and Treatment*, vol. 3, no. 6, pp. 599–609, 2004.

Oh S H, Lee B I, Park T S, Lee S Y, Woo E J, Cho M H, Seo J K, and Kwon O, "Magnetic resonance electrical impedance tomography at 3tesla field strength," *Magnetic Resonance in Medicine*, vol. 51, pp. 1291–1296, 2004.

Oh S H, Lee B I, Woo E J, Lee S Y, Cho M H, Kwon O, and Seo J K "Conductivity and current density image reconstruction using harmonic B_z algorithm in magnetic resonance electrical impedance tomography," *Physics in Medicine and Biology*, vol.48, pp. 3101–3116, 2003.

Ozdemir M S, Eyuboglu B M, and Ozbek O, "Equipotential projection-based magnetic resonance electrical impedance tomography and experimental realization," *Physics in Medicine and Biology*, vol. 49, pp. 4765–4783, 2004.

Park C, Park E J, Woo E J, and Kwon O, "Static conductivity imaging using variational gradient bz algorithm in magnetic resonance electrical impedance tomography," *Physiological Measurement*, vol. 25, pp. 257–269, 2004.

Park C, Kwon O, Woo E J, and Seo J K, "Electrical conductivity imaging using gradient bz decomposition algorithm in magnetic resonance electrical impedance tomography (mreit)," *IEEE Transactions on Medical Imaging*, vol. 23, no. 3, pp. 388–394, 2004.

Surowiec A J, Stuchly S S, Barr J R, and Swarup A, "Dielectric properties of breast carcinoma and the surrounding tissues," *IEEE Trans. on BME*, vol. 35, no. 4, pp. 257–263, 1988.

Rec 4/17/06

In Vivo MRI Electrical Impedance Tomography (MREIT) of Tumors

L. Tugan Muftuler, Mark J. Hamamura, Ozlem Birgul, and Orhan Nalcioglu
John Tu & Thomas Yuen Center for Functional Onco-Imaging, University of California, Irvine

Correspondence should be addressed to: L. Tugan Muftuler
Tel: (949) 824 6290
e-mail: muftuler@uci.edu

Running title: *In Vivo* Magnetic Resonance Electrical Impedance Tomography
Keywords: MREIT, Electrical Impedance Tomography, MRI, cancer imaging

Abbreviations:
MRI: Magnetic Resonance Imaging
EIT: Electrical Impedance Tomography
MREIT: Magnetic Resonance Electrical Impedance Tomography
FEM: Finite Element Method
EIS: Electrical Impedance Scanning
OPAMP: Operational Amplifier
SVD: Singular Value Decomposition
NEX: Number of Excitations
SMM: Sensitivity Matrix Method

Acknowledgements: This research was supported in part by grants NIH R01 CA114210, DOD DAMD17-02-1-0326 and DOD W81XWH-04-1-0446.

ABSTRACT

A significant increase in electrical conductivity of neoplasticities compared to healthy tissues and benign formations has been reported in several studies. We previously reported preliminary results with MR based Electrical Impedance Tomography (MREIT) on several phantoms and a single animal. In the presented study, we applied the technique on ten tumor-bearing rats and collected MREIT images to investigate the potential of MREIT for characterizing malignant tumors. Results show that the tumors had significantly higher mean conductivity compared to the mean of conductivity in the rest of the body. Although heterogeneity of conductivity was observed in the tumor, the mean was still higher than the background.

INTRODUCTION

Several *in vitro* studies have shown that the electrical impedance of malignant tissues is significantly higher than those of normal and benign tissues (1, 2). Therefore, *in vivo* impedance imaging of suspicious lesions has the potential to improve the sensitivity and specificity of detecting malignant tumors. Imaging of conductivity distribution can be achieved by Electrical Impedance Tomography (EIT) in which weak electrical currents are injected into or induced in the body and surface voltage measurements are made to reconstruct a conductivity image (3). However, in this technique a limited number of measurement electrodes are placed on the outer surface. This results in poor, non-uniform spatial resolution due to low sensitivity of the voltages to conductivity changes in the interior regions (4)

Imaging conductivity distribution for diagnosing cancer has been proposed by several researchers (5, 6). Cherepenin *et al* proposed a conventional EIT system for breast cancer screening, while Malich *et al* used a newly developed instrument called Electrical Impedance Scanning (EIS). In EIS, electrical currents are injected to the body by a single probe held by the patient and an electrode array placed over the breast is used to measure the distribution of currents on the surface of the breast. This information is used to estimate the distribution of conductivity under the electode array. Although these techniques proved to be useful, both suffer from poor spatial resolution and poor sensitivity to deeper structures.

Magnetic Resonance-Electrical Impedance Tomography (MREIT) has been recently introduced, in which weak electrical currents are injected into the tissue and the resulting perturbations in magnetic field are measured using phase information in MR images. The conductivity distribution inside the body is reconstructed from these magnetic field measurements (7, 8, 9). Unlike conventional EIT, MREIT technique provides measurements from inside the object on a uniform, high resolution grid. This provides uniformly distributed high spatial resolution conductivity images.

Several MREIT studies using biological tissue phantoms have been previously reported (10, 11, 12). However, these studies were done on *in vitro* samples using injected current levels of 12 mA and above. For any *in vivo* study, these current levels are substantially higher than biologically safe current limits and will certainly cause involuntary muscle twitching even if they do not harm the animal. In some of our experiments, we have observed involuntary muscle twitching even at current levels as low as 2mA, if the electrodes are placed near a major nerve bundle by coincidence. In those cases the experiment is immediately stopped and electrodes relocated to avoid any discomfort to the animal.

We have recently reported our preliminary studies with phantoms as well as one *in vivo* experiment (13). Here, we present the results of MREIT performed on ten animals. Parameters like variance and mean in the tumor versus the rest of the body were investigated. The goal is to verify the potential of MREIT to aid in the diagnosis of tumors.

METHODS

Data were collected using a 4T whole body MRI magnet (Magnex Scientific Inc., UK), which is interfaced with a MRRS console (Magnetic Resonance Research Systems, Guildford, UK) that has broadband RF transmit and receive channels. The system is equipped with a whole body gradient coil set (Tesla Eng. UK), which provides up to 3G/cm gradient fields. The clear bore of the magnet is 650mm in diameter with the gradient tube. The system also includes a 13 channel room-temperature high-order shim system with MXA-13-4 shim power supply (Resonance Research, Billerica, MA) to minimize field inhomogeneities. A 16 leg, quadrature, high-pass birdcage coil was designed and built in-house for the MREIT experiments. This coil has 10 cm diameter and 18 cm length, which is suitable to image large size sprague-dawley rats used in the experiments.

Pulse sequence

The pulse sequence used for the MREIT experiments employs a train of 180^0 RF pulses following a 90^0 RF pulse (Fig.1). No spatial encoding gradients were applied between the 180^0 RF pulses and the data was collected with a single read-out gradient only after the last 180^0 RF pulse. Alternating electrical currents were injected to the animals in the form of burst sine wave pulses in synchrony with the RF pulse train where polarity of current changed after each 180^0 RF pulse. The duration of each 180^0 RF pulse was 1.3ms. A similar sequence was proposed by Mikac *et al* to obtain an image of electric currents inside an object (14).

Fig.1

These currents flowing inside the animal's body generate magnetic fields. The component of the magnetic field that is parallel to the main static field (z-component) introduces a phase shift that accumulates over each half-cycle of the sine wave. The signal equation for MREIT is given as:

$$s(u,v) = \iint M(x,y)\, e^{j\theta(x,y)}\, e^{j(xu + y\,v)}\, e^{j\gamma \int_0^t (b(x,y)\cos(\omega t))\, dt}\, dxdy \quad [1]$$

Here, *M(x,y)* is the magnetization of protons at *(x,y)*. and the T1, T2 decays are ignored to simplify the equation (they can be considered as constant weighting factors, thus *M(x,y)* accounts for the proton density as well as the T1 and T2 weighting). The constant phase shifts due to various sources such as static field inhomogeneity and other hardware related phase delays are all summarized in the phase term $\theta_{(x,y)}$; γ is the gyromagnetic ratio, and *u* and *v* are the spatial frequencies given by $u=\gamma*G_x*T_{Gx}$ and $v=\gamma*G_y*T_{Gy}$, where T_{Gx} and T_{Gx} are the durations of the gradient pulses Gx and Gy, respectively. Therefore, in the MREIT image the total phase accumulated at a pixel at location *(x,y)* due to the magnetic field generated by injected currents is:

$$\varphi(x,y) = 4\cdot\gamma\cdot N\cdot b(x,y) / \omega \quad [2]$$

where N is the number of cycles of injected current, ω is the angular frequency and *b(x,y)* is the amplitude of the magnetic field at point *(x,y)* (z-component only) generated by injected currents. This phase term in equation 2 can be easily measured from the MREIT images. Therefore, the z-component of the magnetic field distribution can be calculated.

Since the constant phase term $\theta_{(x,y)}$ is unknown, the data has to be collected twice with the polarity of electric current reversed. When the phase of these two MREIT images are subtracted, static phase terms will be eliminated, leaving only the phase term introduced by *b(x,y)*.

MREIT Hardware: Several hardware components were interfaced to the MRI system to perform the experiments. The MRI console controls the whole experiment, which generates the pulse sequence, acquires the incoming data, and synchronizes the external units. The sine waves were produced by an HP ESG-4400B signal generator. These signals were synchronized to the pulse sequence by a TTL pulse generated by the scanner computer. A transconductance amplifier was designed and built using three LM741 OPAMP circuits to convert the voltage from the signal generator into a current output. This circuit is described in detail in (15), which was replicated from (16). The output current was calibrated to 1ma/2V and an independent measurement of current was not used. This experimental was described in more detail in (13). After data collection, raw MRI data (k-space) was uploaded to another computer for off-line processing.

MREIT Conductivity image reconstruction

A relationship between the conductivity distribution inside an object and the measured magnetic field has to be established to be able to reconstruct images of conductivity. If all three orthogonal components of the magnetic field were known, Maxwell's equations could have been utilized to calculate the current density distribution. However, this is only possible by rotating the object in three orthogonal directions inside the MRI system which will not be practical with human subjects. Even with small animals, rotation

would introduce problems with registration of measurements taken with different orientations of the body under investigation. The geometry of the soft tissues would deform due to gravity, complicating the registration further. Moreover, a larger RF coil had to be used, which would reduce the SNR. Therefore, a method was adopted that uses only the z-component of the magnetic field to calculate the conductivity distribution (7, 8).

In order to calculate the relationship between the conductivity distribution of an object and the magnetic fields generated by currents flowing inside that object, we first start with the calculation of the electric potential distribution $\phi(x,y,z)$ in the imaging slice. This is calculated by solving Poisson's equation with Neumann boundary conditions, which is given by:

$$\nabla \cdot (\sigma \nabla \phi)(x,y) = 0 \qquad (x,y) \in D$$
$$\sigma \frac{\partial \phi}{\partial n} = \begin{cases} J \text{ on positive current electrode} \\ -J \text{ on negative current electrode} \\ 0 \text{ elsewhere} \end{cases} \qquad [3]$$

where σ is the electrical conductivity, ϕ is the electric potential and ***D*** is the slice of object to be imaged. The above problem is a nonlinear equation since the electric potential itself is also conductivity dependent. It is difficult to obtain an analytic solution for equation 3, therefore numerical methods should be used. In this study, the Finite Element Method (FEM) was used to calculate the distribution of the electric potential. Once ϕ is calculated, the electric field and current density distribution inside the imaging region may be found using the following equations:

$$\vec{E} = -\vec{\nabla}\phi$$
$$\vec{J} = \sigma \vec{E} \qquad [4]$$

Finally, the magnetic flux density generated by this ohmic current can be calculated using the Biot-Savart law. The magnetic field can be written in terms of the differential current element $Id\vec{l}$ as,

$$\vec{B}(x,y,z) = \frac{\mu_o}{4\pi} \int \left(\frac{Id\vec{l} \times \vec{R}}{R^3} \right) \qquad [5]$$

where μ_o is the permeability constant and $\vec{R}$ is the vector from the source point at *(x', y', z')* to the field point *(x, y, z)*. Using equations 3-5, one can solve the *forward problem* where the magnetic field is calculated for an initial conductivity distribution. In order to solve the *inverse problem* of finding the conductivity image from the magnetic field measurements, the *sensitivity matrix method* (SMM) was employed, in which a linear relationship between the conductivity perturbations, $\Delta\boldsymbol{\sigma}$, and magnetic field perturbations, $\Delta\mathbf{B}$, was assumed (8). This relationship is given as:

$$\begin{bmatrix} \Delta B_1 \\ \Delta B_2 \\ \vdots \\ \Delta B_m \end{bmatrix} = \begin{bmatrix} \frac{\partial B_1}{\partial \sigma_1} & \frac{\partial B_1}{\partial \sigma_2} & \cdots & \frac{\partial B_1}{\partial \sigma_n} \\ \frac{\partial B_2}{\partial \sigma_1} & \frac{\partial B_2}{\partial \sigma_2} & \cdots & \frac{\partial B_2}{\partial \sigma_n} \\ \vdots & \vdots & \ddots & \vdots \\ \frac{\partial B_m}{\partial \sigma_1} & \frac{\partial B_m}{\partial \sigma_2} & \cdots & \frac{\partial B_m}{\partial \sigma_n} \end{bmatrix} \bullet \begin{bmatrix} \Delta\sigma_1 \\ \Delta\sigma_2 \\ \vdots \\ \Delta\sigma_3 \end{bmatrix} \quad [6]$$

$$\mathbf{\Delta B_z = S \cdot \Delta\sigma}$$

Here, $\mathbf{\Delta B} = \mathbf{B}_{meas} - \mathbf{B}_i$ and $\mathbf{\Delta\sigma} = \mathbf{\sigma}_{calc} - \mathbf{\sigma}_i$; where $\mathbf{\sigma_i}$ is the initial estimate of the conductivity distribution and $\mathbf{B_i}$ is the field distribution corresponding to $\mathbf{\sigma_i}$. For most cases, a uniform distribution is assumed for $\mathbf{\sigma_i}$. B_{meas} is the magnetic field measurements obtained from MRI. If there are *n* conductivity elements in the FEM and *m* measurement points from MREIT data, then $\mathbf{\Delta\sigma}$ is an *n*x1 vector, $\mathbf{\Delta B}$ is an *m*x1 vector and the *sensitivity matrix* **S** is an *m* x *n* matrix. The entry of the sensitivity matrix at i^{th} row and j^{th} column denotes the change in the i^{th} field measurement due to a small change in conductivity of the j^{th} element. The sensitivity matrix can be calculated using either a numerical or a semi-analytical approach. In the numerical approach, each column of the sensitivity matrix is calculated separately by solving the forward problem by changing the conductivity of a single element. This approach requires the repetitive solution of the forward problem and increases the execution time. For faster reconstruction, the semi-analytical method was used for the calculation of the sensitivity matrix which was described in (8). Once **S** is calculated, the conductivity distribution can be approximated by:

$$\mathbf{\Delta\sigma = S^{-1} \cdot \Delta B} \quad [7]$$

Since SMM approximates the relationship between perturbations in conductivity and perturbations in B_z (z component of magnetic field density) with a linear matrix equation, this reconstruction method provides accurate results only for small conductivity perturbations. On the other hand, several researchers reported substantial changes in conductivity between normal and malignant tissues (1, 2). Therefore, SMM will tend to underestimate the actual conductivity contrast. In this study, an iterated SMM with Tikhonov regularization was used to solve the nonlinear imaging problem and also to reduce the artifacts, especially near the boundaries close to the electrodes. The solution to equation 7 is found by solving the least squares problem:

$$\min \| \mathbf{S\Delta\sigma - \Delta b} \| \quad [8]$$

where $\| \cdot \|$ is the L_2 norm. For most cases, the problem above is ill-conditioned and a regularization method that computes an approximate solution through a regularization parameter is required. In this study, the linear equation was solved using the conjugate gradient method with Tikhonov regularization, where $\mathbf{\sigma}_{calc}$ was found by introducing an additional term to the cost function:

$$\min \{ \| \mathbf{S\Delta\sigma - \Delta b} \|^2 + \lambda \| \Delta\sigma \|^2 \} \quad [9]$$

where λ is the regularization parameter. This approach attempts to minimize the residual norm while penalizing large perturbations in the solution ($\Delta\boldsymbol{\sigma}$).The regularization parameter λ was chosen such that the calculated B_z generated by the reconstructed conductivity distribution was closest to the magnetic flux density measured by MREIT:

$$\min_{\lambda}\{\left\| B_{final} - \left[B(\sigma)\right]_{\sigma=\sigma_{calc}(\lambda)} \right\|\} \qquad [10]$$

Once $\boldsymbol{\sigma}_{calc}$ is calculated, the change in conductivity $\Delta\sigma$ was checked against a predefined threshold, then this σ_{calc} was assigned as the new, updated σ_i, and the process was iterated.

In vivo experiments:

Ten rats bearing malignant tumors were imaged in this study. Data sets from two animals were discarded due to severe motion artifacts. The tumors were either R3230AC tumor grafts or induced by the carcinogen ENU (N-ethyl-N-nitrosourea) (17). Animals were anesthetized by IV injection of ketamine and xylazine prior to imaging. All procedures were approved by the IACUC.

An animal holder was prepared from acrylic sheets for *in vivo* MREIT experiments (Fig.2). This holder helped keep the animal and the electrodes stationary during imaging. This structure also enabled placement of the electrodes in consistent positions across different animals as well as on the same animals for potential longitudinal studies. 5mm×5mm self-adhesive copper foil was taped over hollow acrylic tubes as electrodes. Those tubes were filled with CuSO4 solution as an MRI marker to detect the electrode positions precisely in the images. Precise localization of electrode positions is essential to enter correct boundary conditions for accurate reconstruction of impedance images. Otherwise, artifacts were seen especially along the periphery, near the electrodes. Thin copper wires that carried the electrical current ran along these tubes, and the tubes were aligned in z-direction to minimize interference from the magnetic fields generated by current in the wires. The electrodes were covered with a thin layer of conductive gel to provide good electrical contact. The skin areas where the electrodes would be placed were shaved for better conductance.

Fig.2

Structural images were collected using a T2 weighted SE sequence. Scan parameters were: data matrix = 128X128, FOV = 10cm, slice thickness = 4mm, with 2mm gap. TR = 3s, TE = 50ms and NEX = 2 were used. MREIT images were collected using the outlined pulse sequence with TR=1000ms, TE=30ms, and NEX=2, 64X64 data matrix, FOV = 10cm, slice thickness = 4mm with 2mm gap. Two cycles of 100Hz current with 1mA peak was applied for all studies. One set of MREIT data was collected by applying the current between one pair electrodes. Since there were four electrodes, subsequent MREIT data were collected by applying current from different pairs, generating six different current profiles (fig 3). As

Fig.3

mentioned previously, data were collected with both ± polarities of the currents to eliminate phase accumulation from other sources.

In two of the rats, we have also collected MRIET data with current amplitudes of 0.5, 1 and 2mA.

Results

Fig.4 shows T2 weighted MRI and MREIT images of six rats. Tumor areas show increased conductivity depicted with yellow-red colors (see colorbar). On the MREIT images of the animals, separate ROIs (region of interest) were drawn over the tumor region and the rest of the body and the mean conductivity values in these ROIs were calculated. Since MREIT yields relative conductivity values, the ratio of mean conductivities $\sigma_{tumor}/\sigma_{body}$ was calculated for each animal and the graph is shown in Fig.5. It was found that the average of these conductivity ratios pooled over eight animals was 2.17. ROIs were drawn manually based on the tumor observed in T2 weighted MRI images. We have also calculated the ratio of standard deviation to mean conductivity in each tumor region, which may be an indication of *conductivity heterogeneity* inside the tumor volume, rather than SNR (Fig.6). As seen from these figures, consistent results were obtained from these eight animals. Average conductivity increased by roughly 2.2 times in the tumor compared to the rest of the body. The conductivity varied typically between 10% and 20% within the tumor. In two of the rats, from which we have collected MRIET data with current amplitudes of 0.5, 1 and 2mA, highly consistent results were seen especially between 1 and 2mA cases. For example, when MREIT images of 1mA and 2mA cases were subtracted, the mean of the residual was only 1.3% of the mean conductivity in the whole slice. In the case of 0.5mA vs 1mA, the mean of the residual was 12%. Since MREIT gives relative conductivity distributions, the reconstructed conductivity values have an arbitrary scaling; therefore the mean of each MREIT image is scaled to the same value before subtraction.

Fig.4

Fig.5, 6

Discussion

In this study, it has been demonstrated that MRI based impedance imaging has the potential to investigate malignant tumors *in vivo*. This method can be used to identify and characterize neoplasticities, which are known to possess higher electrical conductivity with respect to healthy tissues and benign formations. Higher conductivity inside the tumor was observed consistently in all the animals imaged. Moreover, it was observed that the method was sensitive enough to reveal conductivity heterogeneity in tumors. The same heterogenous structure was observed at different current levels in the same animal, thefore the variations were not random noise. There is still possibility that some systematic errors in data acquisition or reconstruction might have caused such consistent variations. Even though such patterns were not observed in phantom studies, the much more complex structure of the animal might have amplified such systematic errors. This needs to be investigated further.

We have previously carried out extensive phantom studies to optimize the method and assess the spatial resolution, contrast and linearity (13). More robust reconstruction with regularization was developed to minimize artifacts. Software correction algorithms were developed to minimize electrode localization errors, which helped reduce boundary artifacts.

Although the animal model of breast cancer used in this study is a suitable one to perform preliminary studies of *in vivo* MREIT, it also introduced motion artifact problems. This could be easily avoided in actual human studies. In breast imaging, the breasts are stationery and chest motion can be kept outside the breast images by selecting phase encoding in the left-right direction. However, in future tests with animal models, we plan to utilize motion correction schemes such as navigator echoes to minimize the errors caused by motion. Moreover, the abdominal region of a rat is a more complicated structure compared to a woman's breast, when all the internal organs and their inherent motion are considered. Therefore, we expect the MREIT images to be more accurate in potential applications of MREIT on human breast.

The quality and accuracy of conductivity images can be further improved by utilizing 3D FEM based reconstruction. Some of the residual noise or artifacts in the conductivity images could be due to the superposition of magnetic fields generated by currents flowing outside the imaging slice. This can only be modeled by 3D FEM and reconstructed accurately, which is currently being developed.

At this stage the technique may not be used as a standalone diagnostic tool; but it could provide useful information in characterizing the tumor, once a suspicious lesion is detected by other methods. Physiological and structural changes in tumors that lead to such changes in conductivity will be investigated in future studies. Note that good quality MREIT images were collected with biologically safe electrical current levels. To the best of our knowledge, our research group is the only one to demonstrate potential use of MR based impedance imaging in diagnosing or characterizing tumors. The method is still in its early development stages. Further refinements of this technique could improve accuracy more and may reveal important information about the tumor characteristic that cannot be observed with other techniques.

References

1. A. J. Surowiec, S. S. Stuchly, J. R. Barr, and A. Swarup, "Dielectric Properties of Breast Carcinoma and the Surrounding Tissues," *IEEE Trans. on BME*, *35*, 257- 263, (1988).
2. Jossinet J "The impedivity of freshly excised human breast tissue" *Physiol. Meas*. 19 61-75 (1998).
3. Barber DC, Brown BH "Applied potential tomography". *J. Phys. E.: Sci. Instrum.* 17: 723-33, (1984).
4. Seagar A D, Barber D C and Brown B H "Theoretical limits to sensitivity and resolution in impedance imaging" *Clin. Phys. Physiol. Meas*. 8 A13-31 (1987).
5. V. Cherepenin, A Karpov, A Korjenevsky, V. Kornienko, A. Mazaletskaya, D. Mazourov, and D Meister, "A 3D Electrical Impedance Tomography (EIT) System for Breast Cancer Detection," *Physiological Measurement*, *22*, 9-18, (2001).
6. A. Malich, T. Boehm, M. Facius, M. G. Freesmeyer, M. Fleck, R. Anderson, and W. A. Kaiser, "Differentiation of Mammographically Suspicious Lesions: Evaluation of Breast Ultrasound, MRI Mammography and Electrical Impedance Scanning as Adjunctive Technologies in Breast Cancer Detection," *Clinical Radiolody*, *56*, 278-283, (2001).
7. Y. Z. Ider and O. Birgul, "Use of the magnetic field generated by the internal distribution of injected currents for Electrical Impedance Tomography (MR-EIT)" *Elektrik, Turkish Journal of Electrical Engineering and Computer Sciences*, *6*, 215-225, (1998).
8. O. Birgul, B. M. Eyuboglu, and Y. Z. Ider, "Experimental results for 2D magnetic resonance–electrical impedance tomography (MR-EIT) using magnetic flux density in one direction," *Physics in Medicine and Biology*, *48*, 3485-3504, (2003).
9. S. H. Oh, J. Y. Han, S. Y. Lee, M. H. Cho, B. I. Lee, and E. J. Woo, "Electrical Conductivity Imaging by Magnetic Resonance Electrical Impedance Tomography (MREIT)," *Magnetic Resonance in Medicine*, *50*, 875-878, (2003).
10. Khang H S, Lee B I, Oh S H, Woo E J, Lee S Y, Cho M Y, Kwon O, Yoon J R and Seo J K "Jsubstitution algorithm in magnetic resonance electrical impedance tomography (MREIT): phantom experiments for static resistivity images" *IEEE Trans. Med. Imaging* 21 695-702 (2002).
11. Lee B I, Oh S H, Woo E J, Lee S Y, Cho M H, Kwon O, Seo J K and Baek W S "Static resistivity image of a cubic saline phantom in magnetic resonance electrical impedance tomography (MREIT)" *Physiol. Meas*. 24 579-89 (2003).
12. Oh S H, Lee B I, Woo E J, Lee S Y, Kim T S, Kwon O and Seo J K "Electrical conductivity images of biological tissue phantoms in MREIT" *Physiol. Meas*. 26 S279-88 (2005).
13. Muftuler L T, Hamamura M J, Birgul O, and Nalcioglu O, "Resolution and contrast in magnetic resonance electrical impedance tomography (mreit) and its application to cancer imaging," Technology in Cancer Research and Treatment, vol. 3, no. 6, pp. 599–609, 2004.
14. U. Mikac, F. Demsar, K. Beravs, and I. Sersa, "Magnetic Resonance Imaging of Alternating Electric Currents," *Magnetic Resonance Imaging*, *19*, 845-856, (2001).
15. Baumann BB, Wozny DR, Kelly SK, Meno FM, "The electrical conductivity of human cerebrospinal fluid at body temperature", *IEEE Trans. BME*, 44, 220-223, (1997).
16. Ackmann JJ, "Complex bioelectric impedance measurement system for the frequency range from 5 Hz to 1MHz" *Annl. Biomed. Eng.*, 21, 135-146 (1993).
17. G. Stoica, A. Koestner, and C. C. Capen, "Neoplasms induced with high single doses of N-ethyl-N-nitrosourea in 30-day-old Sprague-Dawley rats, with special emphasis on mammary neoplasia," *Anticancer Research*, vol. 4, pp. 5-12, 1984.

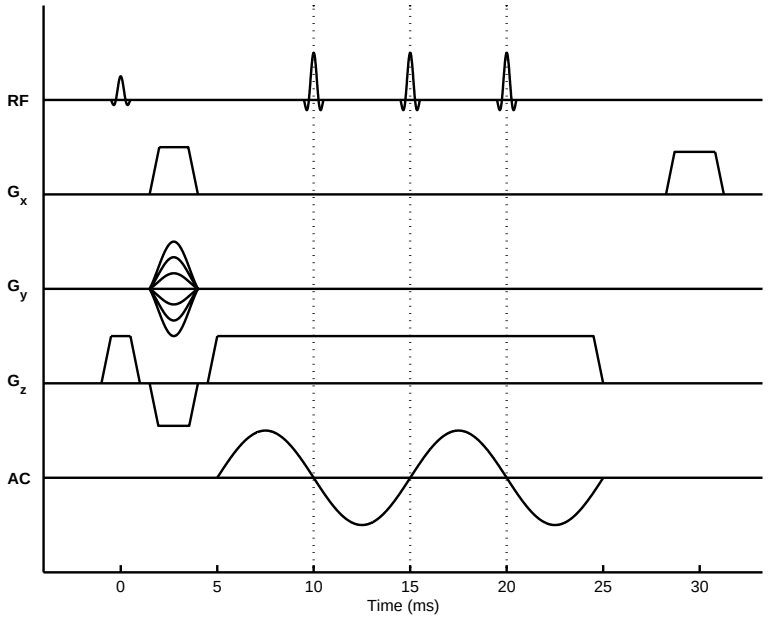

Fig. 1 The MREIT pulse sequence for multi-slice conductivity imaging

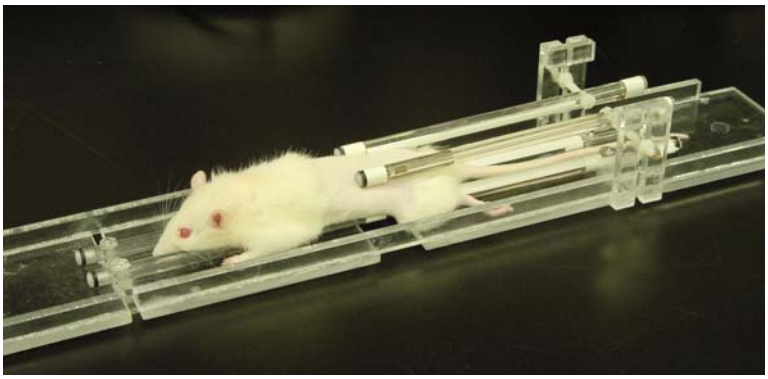

Fig.2. Animal holder with a rat is shown. The electrodes are placed on the tubes and current carrying wires run along those tubes.

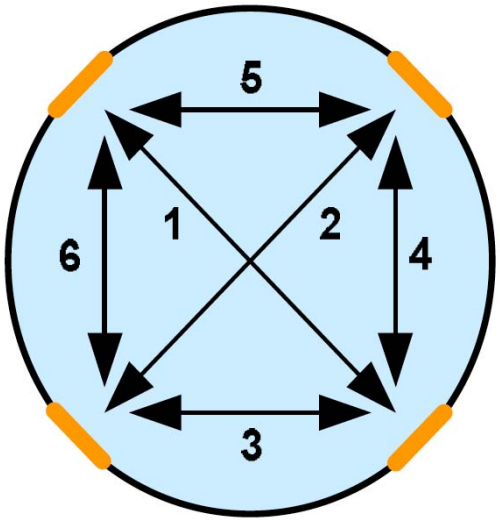

Fig.3. Six different current injection profiles with four electrodes used in the experiments.

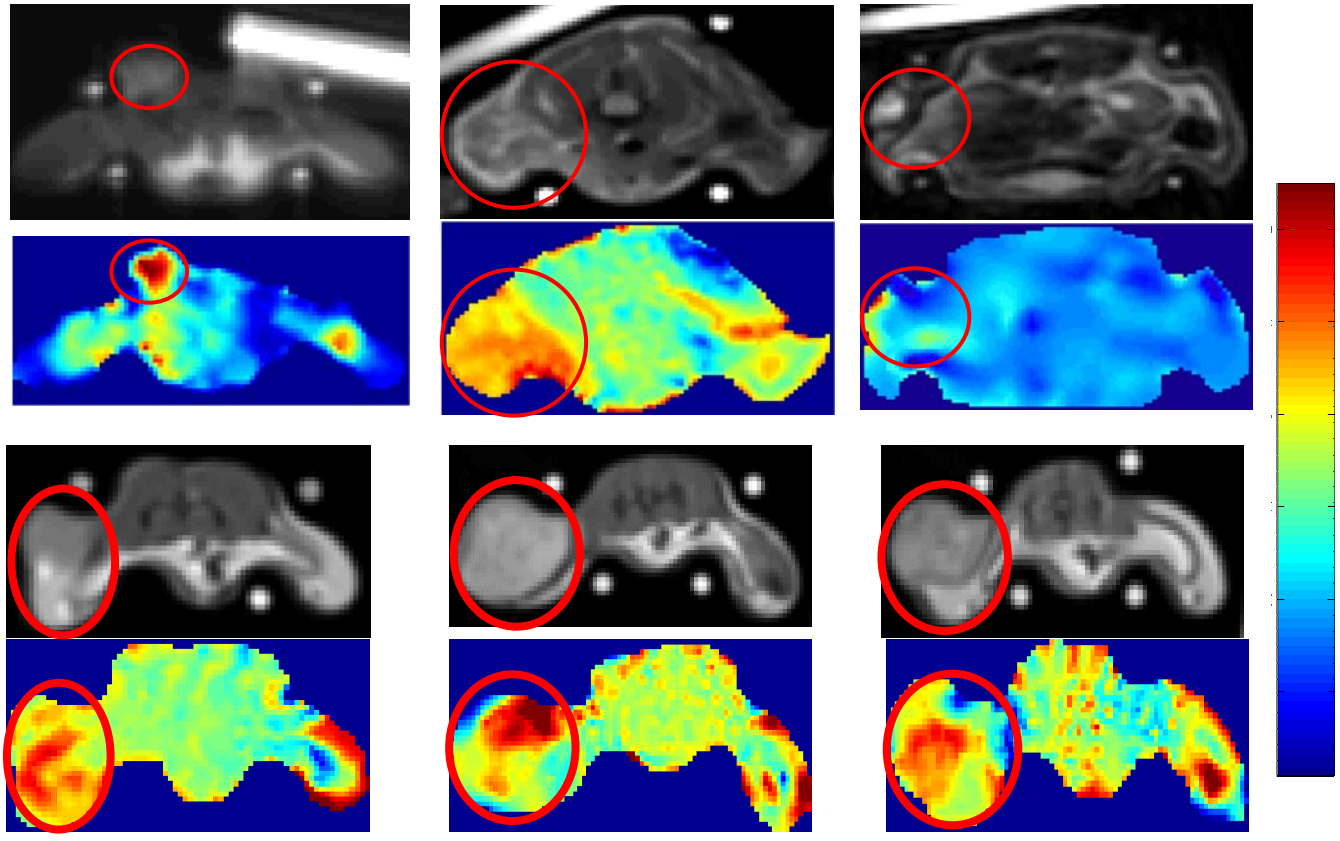

Fig. 4. Structural and MREIT images of six animals are illustrated. Anatomic (T2 weighted) scans are displayed in gray levels and corresponding impedance (MREIT) images are depicted in color right below the T2 weighted images. Each image pair shows axial images from different animals. Tumor areas are circled with red lines. Bright objects outside the animals' body were markers to identify exact location of electrodes.

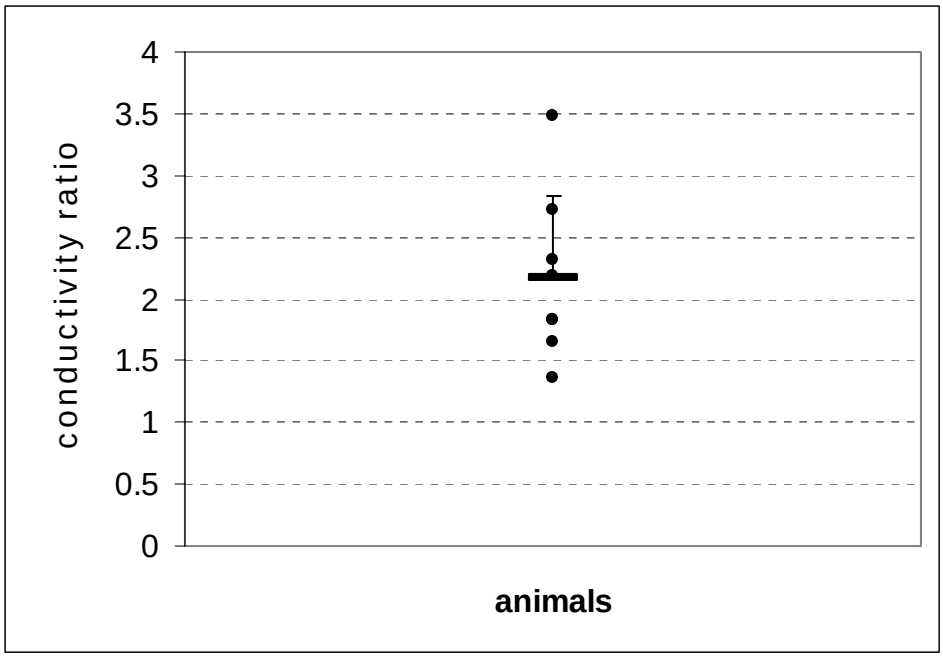

Fig.5. The ratio of mean conductivity in the tumor versus the rest of the body over eight *in vivo* studies. Mean and standard deviation of these measurements are indicated by the dash and the error bar, respectively.

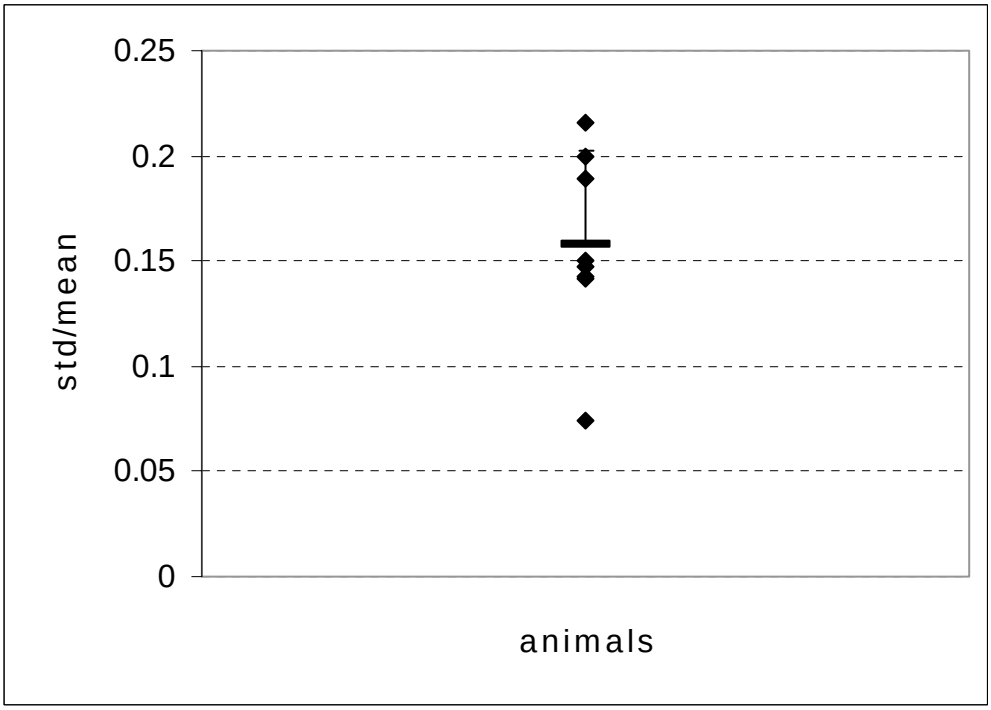

Fig.6. The ratio of standard deviation of conductivity versus its mean in the tumor in eight *in vivo* studies. Mean and standard deviation of these measurement are indicated by the dash and the error bar, respectively.

Reconstruction of Irregular Conductivity Distributions using MREIT at Low Current Levels

O. Birgul[1], L. T. Muftuler[1], M. J. Hamamura[1], O. Nalcioglu[1]
[1]Tu & Yuen Center for Functional Onco Imaging, University of California, Irvine, CA, United States

Purpose

It is possible to detect locations of lesions in breast cancer using techniques such as x-ray mammography or MRI accurately, however, the specificity of current techniques is low [1]. Since the conductivity values of malignant, benign, and normal tissues are significantly different, this information can be used in classification to improve specificity. Magnetic resonance-electrical impedance tomography (MREIT) is an imaging modality that reconstructs conductivity images from magnetic field measurements generated due to a current distribution in a volume conductor. In MREIT low amplitude sinusoidal current is injected into an object and the resulting magnetic field accumulated additional phase in MR images. A modified fast spin-echo sequence is used to measure this magnetic field. These measurements are used to solve the inverse problem of finding the conductivity distribution inside the object using an iterated sensitivity reconstruction algorithm. In most cases, the conductivity distribution is expected to vary within the tumor. There are several phantom studies in literature that assess the performance of MREIT using simple cases but none investigates whether it is capable of detecting complex and nested conductivity distributions, which models the real life cases more accurately. In this study, we used a new criterion for selection of optimum regularization parameter in image reconstruction and showed that it is possible to resolve a 6mm inhomogeneity within an irregular region using lmA peak current.

Methods

Reconstruction of conductivity involves two basic steps. The first step is the measurement of magnetic flux density using magnetic resonance imaging. This step involves MRI data acquisition using a modified spin echo pulse sequence [2] and generation of magnetic flux density images from MRI phase images using scaling. The component of the magnetic flux density in the direction of the main static field of MRI is sufficient in image reconstruction. In the second step, these images are used as input data in the inverse problem of finding conductivity from magnetic field information. Sensitivity based reconstruction algorithm is implemented for the solution of the inverse problem. Uniform conductivity distribution is assumed and sensitivity matrix is calculated analytically [3]. Resulting matrix equation is given as $\Delta\mathbf{b} = \mathbf{S}\Delta\boldsymbol{\sigma}$ where $\Delta\mathbf{b}$ is the difference between measured magnetic flux density and the magnetic flux density corresponding to initial distribution, $\Delta\boldsymbol{\sigma}$ is the change with respect to initial and $\mathbf{S}$ is the sensitivity matrix that gives the relation between changes in magnetic field and conductivity. Including Tikhonov regularization parameter, λ, the matrix equation becomes $(\mathbf{S}^T\mathbf{S} + \lambda\mathbf{I})\,\Delta\boldsymbol{\sigma} = \mathbf{S}^T\Delta\mathbf{b}$ where $\mathbf{I}$ is the identity matrix. The matrix equation is solved for different values of λ using conjugate gradient method and the optimum regularization value is selected as the one minimizing the difference

$$\min_{\lambda} \sum_{i=1}^{m} \left\| B_{meas,i} - B_{calc,i}(\lambda) \right\|$$

where m is the total number of measurement points, B_{meas} is the measured magnetic flux density, and B_{calc} is the flux density calculated using reconstructed conductivity. Calculated conductivity distribution is assigned as the initial value and the steps starting with sensitivity matrix calculation are repeated until the change in conductivity two consecutive iterations are below a defined threshold.

Results

A three region conductivity phantom is generated using agarose and different concentrations of NaCl (Fig 1a). For the background, 1% (g/100mL) agarose and 1% NaCl is used. Agarose amount is kept constant in all regions but NaCl is increased to 2% and 4% for regions II and III respectively. Corresponding conductivity values are measured using a 4 electrode conductivity cell and the true values are found to be 1.54, 2.94, and 5.92mS/cm. Four electrodes are placed around the object giving 6 different current injection profiles. First, high-resolution anatomical images are acquired to determine the exact locations of the electrodes to be used in the image reconstruction (Fig 1b). Since the water content is same in all regions, the irregular region and the 6mm inclusion cannot be seen in the MR image. Then 4 cycles of 1mA (peak) 100Hz current were injected with TR = 1000ms, TE = 50ms, and NEX = 4 and field is measured for 6 cases (Fig 1c). Measurements around the outer ring are masked out to eliminate spurious boundary effects in images reconstruction. Reconstructed conductivity image is given in Fig 1d. where the 6mm region inside the irregular image is resolved. Peak reconstructed values for each region are 1.23, 2.55, and 4.93mS/cm for each region.

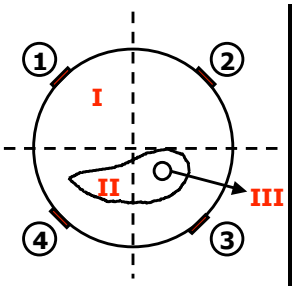

Figure 1a

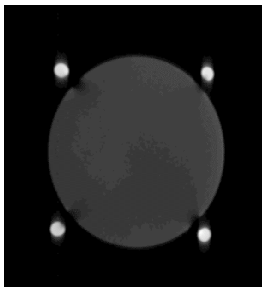

Figure 1b

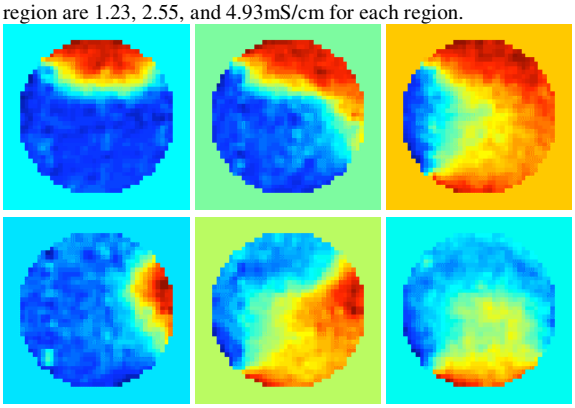

Figure 1c

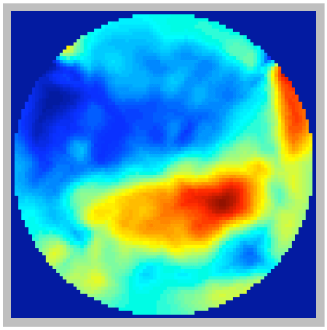

Figure 1d

Figure 1 (a) Schematic of the multi-compartment conductivity phantom (b) MR magnitude images (c) Scaled and masked MR phase images for 6 different current injection case (d) reconstructed conductivity image (red indicating higher conductivity and blue indicating lower conductivity

Discussion

In this study, we have shown that it is possible to reconstruct complex conductivity distributions within an object using MREIT technique and iterated sensitivity reconstruction algorithm. The irregular object and 6mm inclusion, which cannot be seen in the anatomical MR images, are clearly resolved in the conductivity image with 16.7% peak error at current levels which are acceptable for human imaging applications.

References

[1] Malich A, *et. al.*, *Eur. Radiol*, 10: 1555-1561 (2000), **[2]** Muftuler L T, *et. al.,TCRT* December 2004 **[3]** Birgul O, *et. al.* PMB, 48: 3485-2504 (2003)

Acknowledgments

This research is supported in part by Department of Defense Award W81XWH-04-1-0446 and NIH/NCI Award R01 CA114210.

Dynamic MREIT Using Sub-Milliamp Currents

M. J. Hamamura[1], L. T. Muftuler[1], O. Birgul[1], O. Nalcioglu[1]

[1]Tu & Yuen Center for Functional Onco-Imaging, University of California, Irvine, CA, United States

Purpose

In Magnetic Resonance Electrical Impedance Tomography (MREIT), electrical currents are injected into an object and the resulting magnetic flux density distribution measured using MRI. These MRI measurements are then used to reconstruct the conductivity distribution within the object. Previous MREIT studies have focused primarily on reconstructing static conductivity distributions. However, the ability to detect changes in conductivity over time could provide additional diagnostic information. We previously reported on the qualitative monitoring of ion diffusion in agarose gel over four time points using MREIT with 10mA injected currents. In this study, we perform a more thorough monitoring using sub-milliamp injected currents more appropriate for human use.

Methods

For the test phantom, a hollow acrylic disk with an inner diameter of 7cm and thickness of 1cm was filled with 2% agarose and 4mM $CuSO_4$. Within this disk, a smaller circular region of 12mm diameter was filled with 2% agarose, 1% NaCl, and 4mM $CuSO_4$ (Figure 2a). Over time, the NaCl diffused from the smaller region into the background, and the conductivity distribution changed. A linear relationship between conductivity and NaCl concentration (of 1% or less) was found after performing a range of conductivity measurements using the 4-electrode technique. The plane of the disk was placed perpendicular to the main static MRI field. Four copper electrodes each 6mm wide were placed equidistantly along the inner acrylic wall and used to inject currents into the interior region.

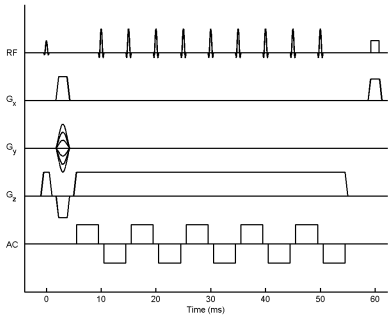

Figure 1. Pulse sequence used in MREIT

A finite alternating current pulse waveform with an amplitude of 900uA was injected into the phantom and the resulting magnetic flux density distribution measured using a modified spin-echo pulse sequence (Figure 2) [*Mikac et al, MRI 19: 845-856 (2001)*]. The scan parameters were TR=500ms, TE=60ms, NEX=4, Matrix=64X64, FOV=10cm, and single slice thickness = 5mm. Data was collected for two different current injection schemes (in pairs of electrodes directly opposite of each other) and used simultaneously in conductivity reconstruction. To reconstruct the conductivity distribution using the MRI measurements, the Sensitivity Matrix Method was utilized [*Birgul et al, Phys Med Bio 48: 3485-3504 (2003)*] in which the relationship between conductivity and magnetic flux density is linearized around an initial conductivity (i.e. uniform distribution) and formulated as a matrix equation. This equation is then solved for the true conductivity distribution using Tikhonov regularization. The resulting conductivity can then be substituted back into the linearized equation as the new, updated initial condition, and the process iterated to improve the reconstruction.

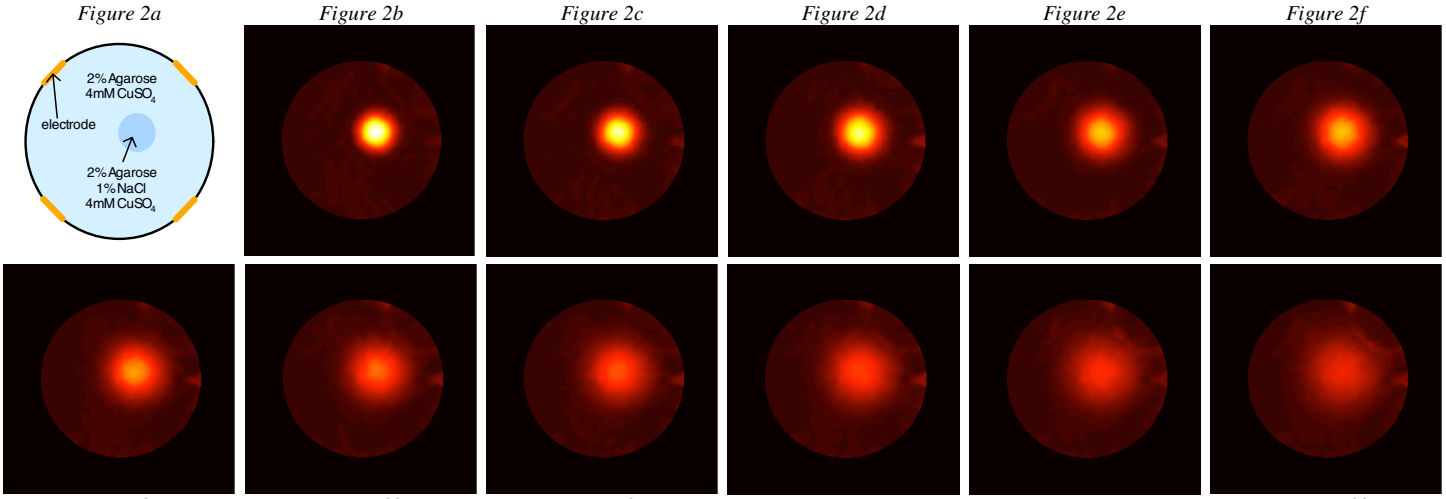

Figure 2a *Figure 2b* *Figure 2c* *Figure 2d* *Figure 2e* *Figure 2f*

Figure 2g *Figure 2h* *Figure 2i* *Figure 2j* *Figure 2k* *Figure 2l*

Figure 2. (a) Schematic of the phantom; (b) Conductivity after 20 minutes; (c) 1 hour; (d) 2 hours; (e) 3 hours; (f) 4 hours;(g) 5 hours; (h) 6 hours; (i) 7 hours; (j) 8 hours; (k) 10 hours; (l) 12 hours

Results

Data was collected at various time points, and the conductivity distributions reconstructed (Figures 2b-l). The resulting images clearly show a change in the conductivity distribution consistent with the diffusion of NaCl from the higher concentration region to the lower concentration region. For a disk of radius a on an infinite plane surface, the theoretical concentration C at the center of the disk is given as $C=C_0(1-\exp(-a^2/4Dt))$. The peak conductivity values were fitted to this equation, and an experimental diffusion constant of $D = 5.8\times10^{-6}$ cm^2 sec^{-1} obtained (Figure 3). This value is smaller than the previously reported measurement of 1.4×10^{-5} cm^2 sec^{-1} [*Schantz et al, Biochem 1: 658-663 (1962)*]. The slower apparent diffusion in this phantom can in part be attributed to its finite shape and confined volume.

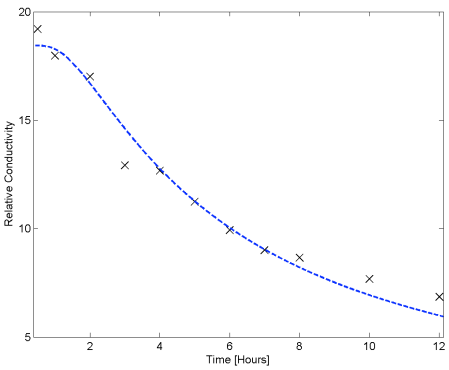

Figure 3. Peak conductivity values

Discussion

The results of this study demonstrate that MREIT can monitor changes in conductivity over time using sub-milliamp injected currents. Validating this ability is a necessary step towards the imaging and monitoring of *in vivo* subjects using MREIT.

Acknowledgement

This research is supported in part by NIH/NCI R01 CA114210, DOD DAMD17-02-1-0326, and DOD W81XWH-04-1-0446a.

Electrode Misalignment Correction Algorithms In Magnetic Resonance Electrical Impedance Tomography

M. J. Hamamura[1], L. T. Muftuler[1], O. Birgul[1], O. Nalcioglu[1]

[1]Tu & Yuen Center for Functional Onco-Imaging, University of California, Irvine, CA, United States

Purpose

In Magnetic Resonance Electrical Impedance Tomography (MREIT) electrical currents are injected into an object and the resulting magnetic flux density distribution measured using MRI. These MRI measurements are then used to reconstruct the conductivity distribution within the object. Many of the reported MREIT reconstruction algorithms utilize numerical calculation of the magnetic flux density for a given conductivity distribution using the boundary conditions applied to the real object. This corresponds to matching the position of the electrodes in the numerical computation to that of the actual position of the electrodes on the object. Near an injecting electrode, there exists a large variation in the magnetic flux density. As a result, any misalignment in the position of an electrode can result in significant errors when calculating the difference between the computed magnetic flux density distribution and the MRI-measured magnetic flux density distribution. Such errors may generate artifacts in the final reconstructed conductivity distribution. In this study, we investigate various correction algorithms to reduce these artifacts.

Method

For the test phantom, a hollow acrylic disk with an inner diameter of 7cm and thickness of 1cm was filled with 2% agarose, 0.1% NaCl, and 4mM $CuSO_4$. Within this disk, a smaller circular region of 12mm diameter was filled with 2% agarose, 1% NaCl, and 4mM $CuSO_4$ (Figure 1). The conductivities of the different regions were measured using the 4-electrode method and found to yield a contrast ratio of 1 to 7.4. The plane of the disk was placed perpendicular to the main static MRI field. Four copper electrodes each 6mm wide were placed equidistant along the inner acrylic wall and used to inject currents into the interior region.

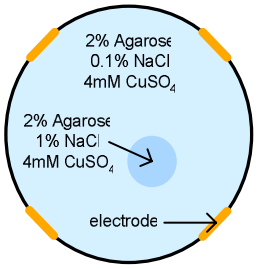

Figure 1. Schematic of the phantom

A finite alternating current pulse waveform with an amplitude of 900uA was injected into the phantom and the resulting magnetic flux density distribution measured using a modified spin-echo pulse sequence (Figure 2) [*Mikac et al, MRI 19: 845-856 (2001)*]. The scan parameters were TR=500ms, TE=60ms, NEX=4, Matrix=64X64, FOV=10cm, and single slice thickness = 5mm. Data was collected for two different current injection schemes (in pairs of electrodes directly opposite of each other) and used simultaneously in conductivity reconstruction. To reconstruct the conductivity distribution using the MRI measurements, the Sensitivity Matrix Method was utilized [*Birgul et al, Phys Med Bio 48: 3485-3504 (2003)*] in which the relationship between conductivity and magnetic flux density is linearized around an initial conductivity (i.e. uniform distribution) and formulated as a matrix equation. This equation is then solved for the true conductivity distribution using Tikhonov regularization. The resulting conductivity can then be substituted back into the linearized equation as the new, updated initial condition, and the process iterated to improve the reconstruction.

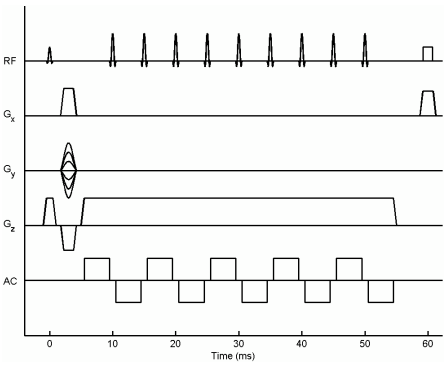

Figure 2. Pulse sequence used in MREIT

Three different electrode misalignment correction algorithms can be implemented during reconstruction. For the first algorithm (MASK), magnetic flux density measurements within 1cm of the electrodes were discarded and not used during reconstruction. For the second algorithm (SHIFT), the position of each electrode assigned during numerical computation was perturbed to find the best location. The difference between the MRI-measured magnetic flux density and the calculated magnetic flux density given the initial condition was minimized as a function of electrode position. For the third algorithm (REG), conductivity perturbations within 1cm of the electrodes were suppressed by a factor of 2 when compared to the rest of the phantom through increased weighting in the Tikhonov regularization.

Contrast = 4.3555

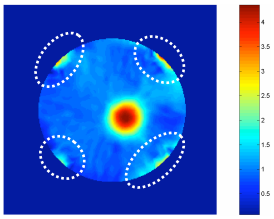

Figure 3a

Contrast = 7.1568

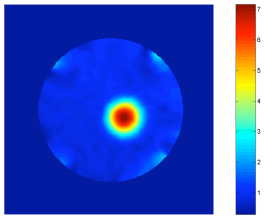

Figure 3b

Contrast = 7.2036

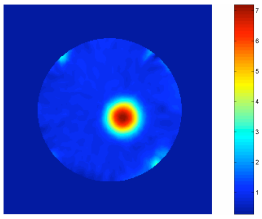

Figure 3c

Contrast = 6.7546

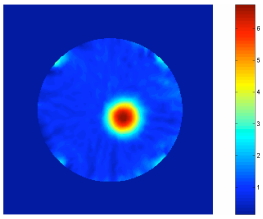

Figure 3d

Contrast = 7.5216

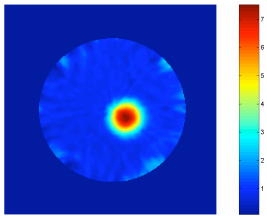

Figure 3e

Figure 3. (a) Reconstructed conductivity distribution using no correction; (b) MASK; (c) SHIFT; (d) REG; (e) all 3 algorithms

Results

Data was collected using a 4T MRI system. Conductivity distributions were reconstructed for various combinations of electrode correction algorithms using 5 iterations of the Sensitivity Matrix Method (Figures 3a-e). For each reconstructed image, the contrast between the high and low conductivity regions was calculated by finding the maximum conductivity value and dividing it by the mean conductivity of the background. The background conductivity was calculated by finding the average conductivity of the phantom excluding a 2cm diameter disk centered on the high conductivity region.

Discussion

The results of this study indicate that electrode misalignment affects the reconstructed conductivity distribution throughout the phantom. Regions next to the electrodes contain artifacts as circled in Figure 3a, while objects in the interior region suffer from diminished contrast. Each of the proposed correction algorithms improves the reconstruction, with the best result occurring when all three methods are applied.

Acknowledgement

This research is supported in part by NIH/NCI R01 CA114210, DOD DAMD17-02-1-0326, and DOD W81XWH-04-1-0446a.

Multiple Current Injection Schemes In Magnetic Resonance Electrical Impedance Tomography

M. J. Hamamura[1], L. T. Muftuler[1], O. Birgul[1], O. Nalcioglu[1]

[1]Tu & Yuen Center for Functional Onco-Imaging, University of California, Irvine, CA, United States

Purpose

In Magnetic Resonance Electrical Impedance Tomography (MREIT) electrical currents are injected into an object and the resulting magnetic flux density distribution measured using MRI. These MRI measurements are then used to reconstruct the conductivity distribution within the object. In order to determine the conductivity distribution uniquely, data from at least two different current distributions satisfying $|\mathbf{J}_1(x,y) \times \mathbf{J}_2(x,y)| \neq 0$ must be acquired [*Kwon O. et al, IEEE Trans on BME 49: 160-167 (2002)*]. Typically, two electrodes are used to provide one current distribution, and two additional electrodes are used to provide a second current distribution, for a total of four electrodes and two current injection schemes. However, with four electrodes, one can apply up to six different current injection schemes using different pairs of electrodes (Figure 1). In this study, we assess the effects of utilizing these additional current injection schemes.

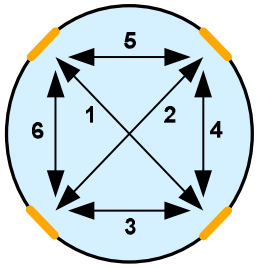

Figure 1. Multiple Current Injection Schemes

Method

For the test phantom, a hollow acrylic disk with an inner diameter of 7cm and thickness of 1cm was filled with 2% agarose, 0.1% NaCl, and 4mM $CuSO_4$. Within this disk, a three smaller circular regions each 1cm in diameter were filled with 2% agarose, 1% NaCl, and 4mM $CuSO_4$ (Figure 3). The conductivities of the different regions were measured using the 4-electrode method and found to yield a contrast ratio of 1 to 7.4. The plane of the disk was placed perpendicular to the main static MRI field. Four copper electrodes each 6mm wide were placed equidistant along the inner acrylic wall and used to inject currents into the interior region.

A finite alternating current pulse waveform with an amplitude of 900uA was injected into the phantom and the resulting magnetic flux density distribution measured using a modified spin-echo pulse sequence (Figure 2) [*Mikac et al, MRI 19: 845-856 (2001)*]. The scan parameters were TR=500ms, TE=60ms, NEX=4, Matrix=64X64, FOV=10cm, and single slice thickness = 5mm. To reconstruct the conductivity distribution using the MRI measurements, the Sensitivity Matrix Method was utilized [*Birgul et al, Phys Med Bio 48: 3485-3504 (2003)*] in which the relationship between conductivity and magnetic flux density is linearized around an initial conductivity (i.e. uniform distribution) and formulated as a matrix equation. A separate equation is generated for each current injection scheme, and various combinations of these equations can be combined to solve for the conductivity distribution. The solution is obtained using Tikhonov regularization. The resulting conductivity can then be substituted back into the linearized equation(s) as the new, updated initial condition, and the process iterated to improve the reconstruction.

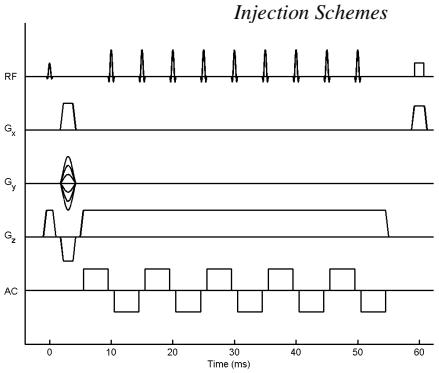

Figure 2. Pulse sequence used in MREIT

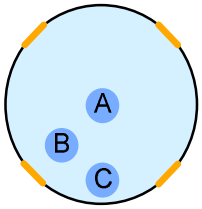

Figure 2. Schematic of phantom

Schemes	1,2	1,2,3	1-6
Region A	6.3398	5.6022	5.2355
Region B	6.3299	5.7407	5.3522
Region C	3.6669	3.6327	3.6439

Table 1. Peak conductivities

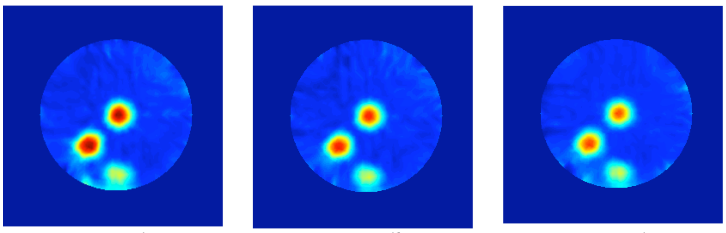

Figure 4a *Figure 4b* *Figure 4c*

Fig 4. Reconstructed conductivity using injection schemes: (a) 1,2; (b) 1,2,3; (c) 1-6

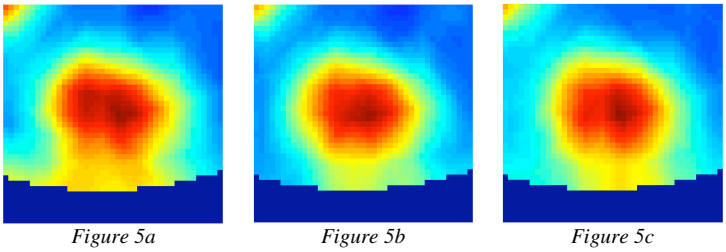

Figure 5a *Figure 5b* *Figure 5c*

Figure 5. Conductivity of Region C for injection schemes: (a) 1,2; (b) 1,2,3; (c) 1-6

Results

Data was collected for each of the 6 current injection schemes. Conductivity distributions were reconstructed for different combinations of data sets using 5 iterations of the Sensitivity Matrix Method (Figures 4a-c). For each reconstructed image, the peak conductivity in each of the three inner regions A, B, and C was found (relative to the background conductivity of 1), and the results compiled in Table 1. A closer view of region C was also extracted (Figures 5a-c).

Discussion

The results indicate that reconstructing periphery regions away from the injecting electrodes presents difficulties, regardless of the current injection schemes used. From inspection of Figure 5, including data from the periphery injection schemes (3-6 in Figure 1) improves the overall shape of object C. In particular, adding scheme 3 provides the largest current density to the region of interest and appears to best improve the spatial distribution. However, overall contrast is best when using only the standard orthogonal injection schemes (1 and 2). Using additional injection schemes further reduces contrast throughout the object.

Selecting which current injection schemes to use requires balancing overall contrast with improved spatial resolution in the periphery regions, and will thus depend on the object to be imaged and the desired information. The increased scan time required to collect data from addition current injection schemes must also be considered.

Acknowledgement

This research is supported in part by NIH/NCI R01 CA114210, DOD DAMD17-02-1-0326, and DOD W81XWH-04-1-0446a.

In Vivo MRI Based Electrical Impedance Tomography of Malignant Tumors

L. T. Muftuler[1], M. Hamamura[1], O. Birgul[1], O. Nalcioglu[1]

[1]John Tu & Thomas Yuen Center for Functional Onco-Imaging, University of California, Irvine, CA, United States

Purpose

Several studies have shown that the electrical impedance of malignant tissues is significantly different from those of normal and benign tissues [1,2]. Therefore, in-vivo impedance imaging of suspicious lesions has the potential to improve the sensitivity and specificity of detecting malignant tumors. MR-Electrical Impedance Tomography (MREIT) has been recently introduced, in which weak electrical currents are injected into the tissue and the resulting perturbations in magnetic field were measured using phase information in MR images. We have reported our preliminary studies with phantoms as well as two *in vivo* experiments [3]. Here, we present the results of MREIT done on eleven animals. Parameters like variance and mean in the tumor versus the rest of the body were investigated. The goal is to verify potential of MR-EIT to aid in the diagnosis of tumors.

Methods

Weak electrical currents that are injected into an object generate magnetic fields, the z-component of which induces additional phase information in MR images. If a modified spin-echo sequence was used with several π pulses applied during the zero-crossings of the alternating current, the phase shift accumulates across these π pulses and is given in the final image as $\varphi(\mathbf{r}) = 4\cdot\gamma\cdot N\cdot b_z(\mathbf{r}) / \omega$, ($\gamma$: gyromagnetic ratio; N: the number of cycles of injected current; $b_z(\mathbf{r})$: the amplitude of current-generated magnetic field at point **r;** ω: angular frequency of the injected current). Here $b_z(\mathbf{r})$ is calculated from the phase $\varphi(\mathbf{r})$ measurements. We have implemented an iterative reconstruction with Tikhonov regularization to reconstruct the conductivity images from $b_z(\mathbf{r})$: $\mathbf{S^T\Delta b_z(r) = (S^TS+\lambda I)\,\Delta\sigma(r')}$. Here the *sensitivity matrix* S is calculated using Finite Element Method; $\Delta b_z(\mathbf{r})$ is the change in magnetic field at point **r** for a given current injection scheme resulting from a change $\Delta\sigma(\mathbf{r}')$ in the conductivity at point **r'**, λ is the *regularization parameter* and **I** is the identity matrix. The details were given in [4].

Data were collected in a whole body 4T MRI system with a MRRS console. Eleven rats were imaged, ten of which were bearing malignant tumors that were either R3230AC tumor grafts or induced by the carcinogen ENU. Animals were anesthetized prior to imaging and all procedures were approved by the IACUC. Two data sets were discarded due to severe motion artifacts. Structural images were collected using T2 weighted SE sequence prior to MREIT images. The data matrix was 128X128, FOV = 10cm, slice thickness = 4mm, with 2mm gap. TR = 3s, TE = 50ms and NEX = 2 were used. MREIT images were collected using the outlined pulse sequence with TR=1000ms, TE=30ms, and NEX=2, 64X64 data matrix, FOV = 10cm, slice thickness = 4mm with 2mm gap. Two cycles of 100Hz current with 1mA rms was applied sequentially through different pairs of four electrodes, generating six different current profiles. Data were collected with both ± polarities of the currents to eliminate phase accumulation from other sources.

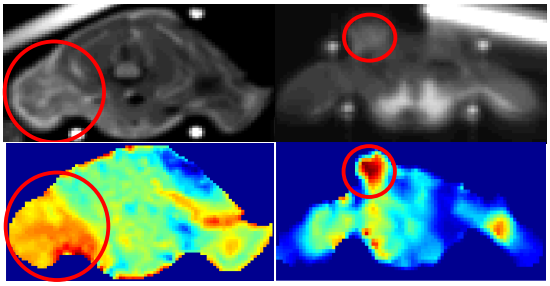

Fig.1. Results from two animals are illustrated. T2 weighted scans are displayed above and corresponding impedance (MREIT) images are depicted in color right below. Tumor areas are marked with red circles.

Results and Discussion

Fig.1 shows T2 weighted MRI and MREIT images of two rats. Tumor areas show increased conductivity depicted with yellow-red colors. On the MREIT images of the animals, separate ROIs (region of interest) were drawn over the tumor region and the rest of the body and the mean conductivity values in these ROIs were calculated. Since MREIT yields relative conductivity values, the conductivity ratio $\sigma_{tumor}/\sigma_{body}$ was calculated for each animal and the graph is shown in Fig.2. It was found that the average of these conductivity ratios was 2.17. ROIs were drawn manually based on the tumor seen in MRI T2 images. We have also calculated the ratio of standard deviation to mean conductivity in each tumor region, which may be an indication of *conductivity heterogeneity* inside the tumor volume, rather than SNR (Fig.3). As seen from these figures, consistent results were obtained from these eight animals. Average conductivity increased by roughly 2.2 times in the tumor compared to the rest of the body. The conductivity varied typically between 10% and 20% within the tumor. In two of the rats, we have also collected MRIET data with rms currents of 0.5, 1 and 2mA. Highly consistent results were seen especially between 1 and 2mA cases. For example, when MREIT images of 1mA and 2mA cases were subtracted, the mean of the residual was only 1.3% of the mean conductivity in the whole slice. In the case of 0.5mA vs 1mA, the mean of the residual was 12%.

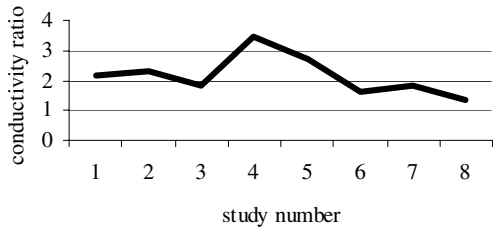

Fig.2. The ratio of mean conductivity in the tumor versus the rest of the body over eight *in vivo* studies.

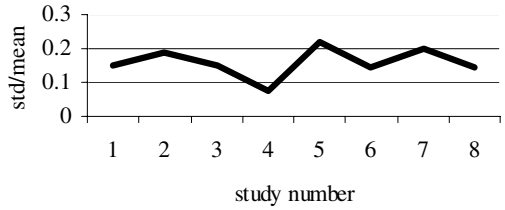

Fig.3. The ratio of standard deviation of conductivity versus its mean in the tumor in eight *in vivo* studies.

In this study, it has been demonstrated that MRI based impedance imaging has the potential to investigate malignant tumors *in vivo*. At this stage the technique may not be used as a standalone diagnostic tool; but it could provide useful information in characterizing the tumor, once a suspicious lesion is detected by other methods to improve specificity. Physiological and structural changes in tumors that lead to such changes in conductivity will be investigated in future studies. Note that good quality MREIT images were collected with biologically safe electrical current levels.

References: [1] Malich A. *et al, Clinical Radiology*,56:278-283, 2001; [2] Silva J.E.D et al.*Med. Biol. Eng. and Comp.*, 38:26-30, 2000; [3] Muftuler LT *et al TCRT* v 3 (2), 599-610, (2004); [4] Muftuler LT et al *Proceedings of ISMRM* 2005, p 2356.

Acknowledgements: This research was supported in part by grants NIH R01 CA114210 and DOD DAMD17-02-1-0326